

Title: Blocking CX3CR1⁺ Tumor-associated Macrophages Enhances the Efficacy of Anti-PD-1 Therapy in Hepatocellular Carcinoma

Running title: CX3CR1⁺ TAMs limit anti-PD-1 therapy efficiency in HCC

Xiaonan Xiang¹, Kai Wang², Hui Zhang³, Haibo Mou⁴, Zhixiong Shi¹, Yaoye Tao⁵, Hongliang Song³, Zhengxing Lian⁶, Shuai Wang⁶, Di Lu², Xuyong Wei⁶, Haiyang Xie^{7,8}, Shusen Zheng^{8,9}, Jianguo Wang^{2*}, Xiao Xu^{1,2*}

¹Institute of Translational Medicine, Zhejiang University School of Medicine, Hangzhou, China. ²Department of Hepatobiliary & Pancreatic Surgery and Minimally Invasive Surgery, Zhejiang Provincial People's Hospital (Affiliated People's Hospital), Hangzhou Medical College, Hangzhou, China. ³The Fourth Clinical Medical College of Zhejiang Chinese Medical University, Hangzhou, China. ⁴Department of Medical Oncology, Shulan (Hangzhou) Hospital, Hangzhou, China. ⁵Department of Hepatobiliary and Pancreatic Surgery, Ningbo Medical Center Li Huili Hospital, Ningbo University, Ningbo, China. ⁶Key Laboratory of Integrated Oncology and Intelligent Medicine of Zhejiang Province, Hangzhou, China. ⁷Division of Hepatobiliary and Pancreatic Surgery, Department of Surgery, The First Affiliated Hospital, Zhejiang University School of Medicine, Hangzhou, China. ⁸NHC Key Laboratory of Combined Multi-organ Transplantation, Hangzhou, China. ⁹Department of Hepatobiliary and Pancreatic Surgery, Shulan (Hangzhou) Hospital, Hangzhou, China.

Xiaonan Xiang, Kai Wang and Hui Zhang contributed equally to this article.

***Corresponding Author:** Xiao Xu, Hangzhou Medical College, Hangzhou, 311399, China, Email: zjxu@zju.edu.cn; Jianguo Wang, Hangzhou Medical College, Hangzhou, 311399, China, Email: wangjianguo8059@zju.edu.cn.

Funding Information: This work was supported by the Key Research & Development Plan of Zhejiang Province (No.2024C03051), the National Key R&D Program of

China (2021YFA1100500), the Major Research Plan of the National Natural Science Foundation of China (No.92159202), the Key Program, National Natural Science Foundation of China (No. 81930016) and the Natural Science Foundation of Zhejiang province (LY22H160046).

Authors' Disclosures: X. Xu reports grants from Zhejiang Provincial Department of Science and Technology, grants from Ministry of Science and Technology of the People's Republic of China, grants from National Natural Science Foundation of China and grants from Natural Science Foundation of Zhejiang province during the conduct of the study. No disclosures were reported by the other authors.

Abstract

The efficacy of immune checkpoint inhibitors (ICI) in the treatment of hepatocellular carcinoma (HCC) remains limited, highlighting the need for further investigation into the mechanisms underlying treatment resistance. Accumulating evidence indicates that tumor-associated macrophages (TAMs) within the tumor microenvironment (TME) have a key role such in immune evasion and treatment resistance. This study explored the role of TAMs in the HCC TME. Our findings reveal that TAMs expressing CX3C motif chemokine receptor 1 (CX3CR1) induced T-cell exhaustion through interleukin-27 (IL-27) secretion in orthotopic models of HCC following treatment with anti-PD-1. Moreover, we identified prostaglandin E2 (PGE2), released by immune-attacked tumor cells, as a key regulator of TAM transition to a CX3CR1⁺ phenotype. To augment the therapeutic response to anti-PD-1 therapy, we propose targeting CX3CR1⁺ TAMs in addition to anti-PD-1 therapy. In conclusion, our study contributes to the understanding of the role of TAMs in cancer immunotherapy and highlights potential clinical implications for HCC treatment. The combination of targeting CX3CR1⁺ TAMs with anti-PD-1 therapy holds promise for enhancing the efficacy of immunotherapeutic interventions in HCC patients.

Synopsis: New approaches are needed to augment efficacy of anti-PD-1 therapy in HCC. The authors uncover a mechanism by which CX3CR1⁺ TAMs promote T-cell exhaustion and limit anti-PD-1 efficacy in HCC models, revealing potential new immunotherapy targets for HCC.

Introduction

Hepatocellular Carcinoma (HCC) is a widespread and deadly malignancy that poses substantial challenges to global health (1). While surgical resection and liver transplantation are currently the primary treatment options, their effectiveness remains limited, with the radical resection rate remaining below 30% and the recurrence rate exceeding 50% (2,3). Additionally, conventional therapeutic approaches including chemotherapy and tyrosine kinase inhibitors (TKI), have shown only limited benefits for HCC patients (4). Therefore, there is an urgent need for innovative strategies to combat HCC and improve patient outcomes.

Immunotherapy, a promising approach in cancer treatment, harnesses the host's immune system to target malignancies. It can be primarily categorized into three main types: immune checkpoint inhibitors (ICI), adoptive cell transfer (ACT) and tumor vaccines (5). ICIs, specifically monoclonal antibodies (mAb) targeting programmed cell death protein 1 (PD-1) or cytotoxic T-lymphocyte-associated antigen-4 (CTLA-4), have garnered substantial interest due to their potent antitumor effects across various malignancies (6). However, their efficacy in HCC remains limited, with a response rate below 20% (7,8). This necessitates the development of innovative strategies to augment the efficacy of ICIs in HCC.

The tumor microenvironment (TME) plays a crucial role in modulating the immune response to cancer (9). Myeloid cells, including tumor-associated macrophages (TAMs) and myeloid-derived suppressor cells (MDSCs), constitute a critical component of this complex ecosystem. These cells can be recruited and modulated by

the tumor, suppressing antitumor immune responses and fostering a milieu conducive to tumor growth (10). Their plasticity enables them to adapt to various TME cues, adopting diverse phenotypes with distinct functional properties (11). For instance, in HCC, hypoxic conditions induce the differentiation of TREM-1⁺ TAMs, which recruit suppressive CCR6⁺ regulatory T cells (Tregs), thereby conferring resistance to anti-PD-L1 therapy (12). Additionally, a subset of TAMs exhibiting enhanced glycolytic capacity inhibits cytotoxic T lymphocyte (CTL) function via upregulation of PFKFB3–PD-L1 signaling (13). Given the pivotal role of tumor-infiltrating myeloid cells, especially TAMs, in shaping the antitumor immune response, they represent a prime topic for cancer immunology research.

In recent years, CX3C motif chemokine receptor 1–positive (CX3CR1⁺) TAMs have garnered attention as pivotal modulators of the TME across multiple cancer types (14). In lung cancer, for instance, CX3CR1⁺ TAMs engage in crosstalk with cancer cells via the CX3CL1/CX3CR1 and CCL2/CCR2 pathways, thereby enhancing tumor migration and invasion (15). Similarly, in colon cancer, these TAMs are associated with neutrophil recruitment, leading to resistance to VEGFR2 inhibition and liver metastasis (16,17). In the context of glioma, CX3CR1⁺ TAMs have been found to suppress antitumor immune responses as they overexpress immune checkpoints such as VISTA and PD-L1 (18). Intriguingly, the presence of CX3CR1⁺ TAMs in tumors appears to impact the efficacy of immunotherapy. Recent studies employing single-cell RNA sequencing (scRNA-seq) have identified these TAMs an immunosuppressive subset with “M2-like” characteristics (19). A reduction in their

numbers has been correlated with successful immunotherapy outcomes (19,20). Conversely, in breast cancer patients resistant to ICI, a notable increase in CX3CR1⁺ TAMs has been observed (21).

In the context of HCC, however, the specific role of CX3CR1⁺ TAMs in immunotherapy remains poorly understood. Our study sheds light on this by exploring the interactions between these TAMs and HCC. We found that prostaglandin E2 (PGE2) released by cancer cells in response to immune attack, upregulated CX3CR1 expression in TAMs. Subsequently, CX3CR1⁺ TAMs were found to induce CD8⁺ T-cell dysfunction through interleukin-27 (IL-27) secretion. These findings provide insights into the mechanisms underlying the immunosuppressive effects of CX3CR1⁺ TAMs in HCC and highlight their potential as therapeutic targets for immunotherapy in this hard-to-treat disease. Targeting CX3CR1⁺ TAMs may therefore overcome immunosuppression and enhance the efficacy of immunotherapy in patients with HCC.

Materials and Methods

Patients' samples

This study enrolled two HCC immunotherapy cohorts, recruited from three independent medical centers: the First Affiliated Hospital of Zhejiang University School of Medicine, the Affiliated Hangzhou First People's Hospital, Zhejiang University School of Medicine and Shulan (Hangzhou) Hospital.

Cohort #1 comprised 14 patients who had undergone anti-PD-1 immunotherapy prior to HCC resection, with tumor tissue slides and preoperative peripheral blood obtained.

Cohort #2 comprised 16 patients with unresectable advanced HCC who received anti-PD-1 immunotherapy. Peripheral blood samples were collected before each treatment cycle. Imaging assessments were conducted every 12 weeks to evaluate the therapy response based on the iRECIST criteria (22). Survival data were collected via telephone follow-up, and recurrence-free survival (RFS) was defined as the interval between surgery and tumor recurrence or metastasis. The final follow-up was completed in December 2021. Demographic, clinical, and histopathological characteristics of the patients are summarized in Supplementary Table S1.

Patient samples were obtained with written informed consent, which was conducted in agreement with the Helsinki Declaration, good clinical practice, and local laws. The study received approval from the Research Ethics Review Committee of the First Affiliated Hospital of Zhejiang University School of Medicine (Approval No. 2019-43), the Affiliated Hangzhou First People's Hospital, Zhejiang University School of Medicine (Approval No. IIT-20220217-0020) and Shulan (Hangzhou)

Hospital (Approval No. KY2021014).

Cell lines

The Hepa1-6 cell line (Cat# CL-0105) was procured from Procell Life Science & Technology Co., Ltd (Wuhan, China) in 2020. The Hepatoma 22 (H22) cell line (Cat# CC9005) was procured from Cellcook Biotech Co., Ltd (Guangzhou, China) in 2020. Both the Hepa1-6 and H22 cell lines underwent reauthentication using short tandem repeat (STR) analysis upon purchase.

The Hepa1-6 cells were cultured in Dulbecco's Modified Eagle Medium (DMEM, 01-052-1A, Biological Industries), supplemented with 10% FBS (10091148, Gibco) and 1% penicillin/streptomycin (P/S, C0222, Beyotime Biotechnology). The H22 cells were cultured in RPMI 1640 medium (01-100-1A, Biological Industries), supplemented with 10% FBS and 1% P/S. All cells were cultured at 37°C in a humidified atmosphere containing 5% CO₂.

Early passage cells were cryogenically preserved in liquid nitrogen. The freshly thawed cells were cultured for approximately 1 week (2–3 passages) prior to use. The total number of passages for each cell line was limited to 20. All cell lines were confirmed to be *Mycoplasma* negative using the Mycoplasma Detection Kit (40612ES25, Yeasen Biotechnology).

To generate luciferase-overexpressing H22 and Hepa1-6 cells (H22-luci and Hepa1-6-luci), lentiviral transduction was performed using U6/Luciferase17&Puro (LV16NC, Genepharma) at a multiplicity of infection (MOI) of 40 in the presence of 2 µg/mL polybrene (40804ES76, Yeasen Biotechnology). The following day, the cell

culture medium was replaced, and 1 $\mu\text{g}/\text{mL}$ of puromycin (60209ES10, Yeasen Biotechnology) was added to the cultures.

Animals

C57BL/6 and BALB/c mice, male, aged 6-8 weeks, were purchased from Zhejiang Academy of Medical Sciences (Hangzhou, China). All mice were maintained in a specific pathogen-free (SPF) animal facility on a 12-hour light/dark schedule with free access to food and water. All animal experiments were performed in accordance with the Institutional Animal Care and Use Committee of the Experimental Animal Welfare Ethics Review Committee, Zhejiang University (Approval No. 21234).

Murine primary cells

Bone marrow–derived macrophages (BMDMs) were isolated from the femur and tibia of 6-8-week-old C57BL/6 mice and cultured in DMEM supplemented with 10% FBS and 40 ng/mL murine M-CSF (315-02, Peprotech) for 7 days prior to subsequent experiments. Murine CD8⁺ T cells were isolated from the spleens of 6-8-week-old C57BL/6 mice utilizing the Dynabeads™ Untouched™ Mouse CD8 Cells Kit (11417D, Invitrogen) according to the manufacturer's protocols. The CD8⁺ T cells were then cultured in RPMI 1640 Medium supplemented with 10% FBS, 1% P/S, and 30 U/mL murine IL-2 (212-12, Peprotech). Activation of the T cells was achieved by stimulation with anti-CD3 and anti-CD28 (16-0031-82, 16-0281-82, Invitrogen) at a 1:2000 dilution for 5 days. Tumor-infiltrating macrophages (CD45⁺CD11b⁺F4/80⁺) and natural killer (NK) cells (CD45⁺NK1.1⁺TCR β ⁻) were harvested from single-cell suspensions of murine HCC tissues by fluorescence-activated cell sorting (FACS) and

cultured in RPMI 1640 Medium supplemented with 10% FBS and 1% P/S. The flow cytometry antibodies used for FACS are detailed in *Flow cytometry staining* section.

All cells were maintained in a humidified incubator at 37 °C with 5% CO₂.

***In vitro* primary cell experiments**

For the immune attack experiment, activated CD8⁺ T cells were co-cultured with tumor cells (Hepa1-6) at a 5:1 ratio for 48 hours. For the TAM–T cell co-culture experiment, naïve CD8⁺ T cells were co-cultured with TAMs in the presence of 1:2000 anti-CD3/CD28 and 30 U/mL murine IL-2, at a ratio of 5:1, and incubated for 72 hours. In certain co-culture experiments, 10 ng/mL recombinant mouse IL-27 (51107-M08H, Sinobiological), 10 µg/mL IL-27-specific monoclonal antibody (16-7285-85, Invitrogen) or 10 µg/mL CX3CR1-specific antibody (TP501, Torrey Pines Biolabs) was added to the co-culture system.

To induce polarization/activation of BMDMs *in vitro*, the following experimental conditions were employed for a duration of 48 hours: (a) stimulation with 50 ng/mL LPS (T11855, TargetMol) and 20 ng/mL IFN-γ (315-05, Peprotech); (b) stimulation with 20 ng/mL IL-4 (214-14, Peprotech) and 20 ng/mL IL-13 (210-13, Peprotech); (c) exposure to hypoxic conditions (1% O₂, 4% CO₂, 95% N₂); (d) culturing in 50% Hepa1-6 supernatant; (e) culturing in 50% supernatant from immune-attacked Hepa1-6 cells; (f) exposure to different concentrations of PGE2 (T5014, TargetMol) in the presence or absence of 10 µM EP2 antagonist (T3306, TargetMol) or EP4 antagonist (TQ0290, TargetMol).

For the adenoviral transfection of BMDMs, adenovirus (Ad5F35) expressing

CX3CR1 (pAd-CX3CR1) and the control (pAd-NC) vector were customized from Wzbio (Jinan China). Adenoviral transfection was conducted at a MOI of 200, following the manufacturer's protocol. To explore the effect of CX3CR1 inhibition on the phenotype or function of BMDMs, we treated control or CX3CR1-overexpressing (CX3CR1^{OE}) BMDMs with 10 µg/mL CX3CR1-specific antibody for 48 hours. The cells were then collected for subsequent testing. Migration assays were performed in 24-well insert plates with 8.0 µm pore size (3422, Corning). After overnight serum starvation (cultured in serum-free medium), 100 µL cell suspensions (in serum-free DMEM) containing 10⁵ control or CX3CR1^{OE} BMDMs were seeded into the upper chamber, and incubated for 10 min at 37 °C and 5% CO₂. Subsequently, 600 µL of different chemotactic agents (serum-free DMEM, 50% Hepa1-6 supernatant or 50% Hepa1-6 supernatant + 10 µg/mL CX3CR1-specific antibody) were added directly to the wells below the transwell inserts. Incubate the plate at 37 °C and 5% CO₂ for 24 h. Nonmigratory cells were removed from the upper surface of the filter. Cells on the lower surface of the membrane were stained by using a crystal violet staining solution (C0121, Beyotime). Cell numbers were counted under Olympus CKX53 optical microscope (Olympus, Japan) and typical images were captured using CellView version 4.10 (BGIMAGING, Hangzhou, China) at 20× magnification.

To track immune cell proliferation and distribution *in vivo*, 2.5 µM CFSE (C34554, Invitrogen) was used to label immune cells (10⁷/ml in PBS). Subsequently, RPMI 1640 with 10% FBS was added to terminate the reaction, followed by 3 washes.

To collect adherent cells cultured *in vitro*, Accutase Solution (03-073-1B, Biological

Industries) was added and incubated at 37°C for 5-10 minutes to detach the cells. The cells were then collected by centrifugation at 300g for 5 minutes at 4°C and used for subsequent experiments.

Orthotopic HCC models

Experiments were conducted with low-passage cultures (< passage 5) of mouse tumor cells. Mice were acclimated for at least 1 week before tumor inoculation. H22-luci cells (10^6) and Hepa1-6-luci cells (10^6) were inoculated orthotopically into the left liver lobes of BALB/c and C57BL/6 mice, respectively, in a 1:1 mixture with Matrigel (354248, Corning) in a volume of 25 μ L. For *in vivo* luciferase imaging, tumor-bearing mice received intraperitoneal (i.p.) administration of 1.5 mg per mouse D-Luciferin Potassium Salt (40902ES03, Yeasen Biotechnology). The IVIS® Spectrum system (Version 4.3.1.0.16427) was utilized for imaging, enabling monitoring of tumor growth.

The treatment protocol for mice included the following: murine anti-PD-1 mAb (BE0146, BioXCell), anti-TIM-3 mAb (BE0115, BioXCell), and control IgG (BE0089, BioXCell) were diluted in PBS, administered i.p. at a dose of 100 μ g every 3 days for a total of 5 doses. Additionally, murine CX3CR1-specific antibody (TP-501, Torrey Pines Biolabs) was diluted in PBS and administered i.p. daily at a dose of 5 μ g for a duration of two weeks. Celecoxib (T0466, TargetMol) was diluted in a solution comprising 10% dimethyl sulfoxide (DMSO), 90% Corn Oil, and was orally administrated at a dose of 10 mg/kg daily for a period of two weeks.

Adoptive cell transfer experiment

For adoptive cell transfer (ACT), we first established Hepa1-6-luci orthotopic HCC tumors as described above. Then we depleted pre-existing phagocytes in tumor-bearing mice by i.p. administration of 200 μ L of neutral clodronate liposomes (F70101C-NL, FormuMax Scientific) 48 hours prior to the ACT. Subsequently, 5×10^5 CFSE-labeled control or CX3CR1^{OE} BMDMs were suspended in 500 μ L PBS, then injected into mouse via tail vein. For CX3CR1 blocking in the ACT experiment, mice were i.p. treated with 5 μ g CX3CR1-specific antibody twice, 1 hour prior and 3 hours after BMDM injection. To monitor the *in vivo* distribution of the BMDMs, *in vivo* fluorescence imaging was performed 24 hours post-ACT.

Winn assay

For the Winn Assay experiments, we first depleted pre-existing phagocytes in C57BL/6 mice by i.p. injection of 200 μ L of neutral clodronate liposomes 48 hours before the experiment. Subsequently, a mixture of BMDMs and Hepa1-6 cells (1:2 ratio), was suspended in 50 μ L of PBS and subcutaneous injected. Tumor growth was monitored every 2 or 3 days by measuring tumor length and width using a caliper. Tumor volume was calculated according to the equation: $0.5 \times (\text{width})^2 \times \text{length}$.

Tissue processing

Murine tumors were collected and placed in pre-cooled PBS to remove necrotic tissue, blood clots, and adjacent normal tissue. Subsequently, for pathological analysis, the tumor tissues were fixed overnight in 10% neutral formalin at 4°C, followed by dehydration and embedding procedures to produce wax blocks suitable for immunohistochemistry (IHC) and immunofluorescence (IF). To assess the cytokine

content within the tumor tissue, the samples were fragmented, homogenized in ice-cold PBS, and centrifuged at 1,200 rpm at 4°C to isolate the supernatant for further analysis (see *ELISA*). For flow cytometry, samples were minced and added to a 6-well plate containing 2 mL of prewarmed RPMI 1640 supplemented with 5 mg/mL of Collagenase IV (LS004188, Worthington) and 1 mg/mL of DNase I (LS004194, Worthington). The mixture was incubated at 37°C on a horizontal shaker at 90-100 rpm for 1 hour. Following enzymatic digestion, the cell suspension was filtered through a 70 µm filter and centrifuged at 300g for 5 minutes at 4°C. The supernatant was discarded, and the immune cell layer was isolated using mouse lymphocyte separation medium (7211011, DAKWE) according to the manufacturer's instructions.

Flow cytometry staining

Single cell suspensions for flow cytometry were prepared as described (see *Tissue processing*). The samples were first stained with viability dyes (423113, Biolegend), followed by washing with FACS buffer (1× PBS, 2% BSA, 2 mM EDTA, 2 mM NaN₃). Subsequently, the cells were incubated on ice with an Fc receptor blocking reagent (101320, Biolegend) to reduce non-specific binding. Next, surface staining antibodies were diluted in FACS buffer and added to the cell samples, followed by a 30-minute incubation on ice in the dark. After rinsing with FACS buffer, the samples were prepared for flow cytometry analysis.

For intracellular cytokine staining, the samples were pre-incubated for 4-6 hours at 37°C with protein transport inhibitors (554724, BD). After surface staining was

completed, the samples were fixed and permeabilized using Fixation/Permeabilization reagent (554714, BD) for 20 minutes at room temperature. Following two washes with Perm/Wash buffer, the cells were treated with intracellular antibodies and incubated on ice for an additional 40 minutes in the dark. Finally, the samples were washed again with Perm/Wash buffer and were ready for flow cytometry analysis. All antibodies used for flow cytometry are listed in Supplementary Table S2.

Flow cytometry & FACS gating

First, based on the FSC-A/SSC-A parameters, immune and non-immune cells can be roughly distinguished. Adherent cells and dead cells were excluded using FSC-A/FSC-H and Zombie Violet stains (423114, Biolegend), respectively. Immune cells were further identified as expressing CD45.

For lymphocytes, CD8⁺ T cells were identified using CD3e and CD8a, and their immune checkpoint expression was profiled with PD-1, TIM-3, LAG-3, and TIGIT stains. Functional CD8⁺ T cells were identified by activation markers CD69, CD107a, and intracellular cytokines IFN- γ , TNF- α , Perforin, and GZMB. To differentiate Natural Killer (NK) cells or NKT cells from the rest of the immune cells, TCR β and NK1.1 was used, with CD69 serving as the markers of their activation.

For myeloid cell analysis, neutrophils were identified as CD11b⁺Ly6G⁺ cells, while dendritic cells, monocytes, and macrophages were characterized as CD11c⁺MHCII⁺, Ly6C⁺F4/80⁻, and Ly6C⁻F4/80⁺ populations, respectively. CX3CR1 expression was utilized to distinguish CX3CR1⁺ and CX3CR1⁻ macrophages.

Flow cytometry was performed on a BD FACSCanto II. FACS was performed on a

Cytek Aurora CS. Data analysis was performed using FlowJo software version 10.10.0 (BD Biosciences, USA). The flow cytometry and FACS strategies are presented in Supplementary Fig. S1.

Single-cell RNA-seq and data analysis

Tumor-infiltrating immune cells (Zombie Violet⁻CD45⁺) were FACS sorted from orthotopic Hepa1-6-luci tumors treated with either IgG or anti-PD-1 (5 tumors per group). Fresh cell pellets in each group were mixed into one sample separately (isotype or anti-PD-1, one replicate each), which were subsequently subjected to scRNA-seq conducted by Genechem (Shanghai, China). Briefly, cell counts and viability were determined using Cell Countess 3 with trypan blue (A50298, Invitrogen). Single-cell suspension was adjusted to 1,000 cell/ μ L in PBS. Sample partitioning and molecular barcoding were done on the Chromium Controller (10 \times Genomics), where cellular suspensions (about 10,000 cells per sample) were loaded together with the Single-cell 5' Gel Beads on a Single-cell 5' chip (PN-1000190, PN-1000286, 10 \times Genomics). RNA from the barcoded cells was subsequently reverse-transcribed and sequencing libraries constructed with reagents from a Chromium Next GEM Single Cell 5' Reagent Kits v2 (PN-1000263, 10 \times Genomics) according to the manufacturer's instructions. Library QC was performed using Agilent 2100 Bioanalyzer (Agilent Technologies, USA), to check the size and purity of the library. The constructed library was sequenced using Illumina NovaSeq 6000 platform (Illumina, USA) to generate 150 bp paired-end reads according to the manufacturer's instructions. The sequencing data were demultiplexed, aligned against

the mouse reference genome mm10, and quantified using Cell Ranger (version 5.0.1). Raw reads of FASTQ format were processed using fastp and the low quality reads were removed to obtain the clean reads (23). After filtering out low-quality cells, red blood cells, and doublets, 9683 (isotype) and 10,149 (anti-PD-1) cells remained for downstream analyses.

Seurat package ([version](#) 4.1.0) was used for cell normalization and cell filtering considering the mitochondrial gene percentage (less than 10%), minimum and maximum gene numbers (200 to 4000). Principal Component Analysis (PCA) and tSNE analysis was used for the single cell to cell relation description. To further investigate immune cell subsets, we selected clusters based on CellMarker database and SingleR annotations (24,25). The TAM populations were labeled based on their expression of myeloid-related markers (*Csf1r*, *Cd68*, *Itgam*), *Cx3cr1* expression was further used to distinguish TAM subpopulations. We performed the Kyoto Encyclopedia of Genes and Genomes (KEGG) pathway analysis between CX3CR1⁺ and CX3CR1⁻ TAM subpopulations, to identify their transcriptomic differences. Further, in order to explore the transcriptomic differences of CX3CR1⁺ TAMs in IgG and PD-1 treated tumors, we used the Gene Set Enrichment Analysis (GSEA) method to compare the differences in CX3CR1⁺ TAMs gene pathway enrichment in two single-cell samples.

Bulk RNA-seq and data analysis

For bulk RNA-seq, samples were adherent Hepa1-6 cells collected from immune attack experiments (see *In vitro primary cell experiments*, n = 5 biological replicates

per group) or magnetically sorted F4/80⁺ cells using F4/80⁺ microbeads (130-110-443, 130-090-544, Miltenyi Biotec) from orthotopic Hepa1-6-luci tumors treated with IgG, anti-PD-1, anti-CX3CR1 or anti-PD-1/anti-CX3CR1 (n = 4 biological replicates per group). Total RNA was extracted using the TRIzol reagent (15596026CN, Invitrogen) according to the manufacturer's protocol. RNA purity and quantification were evaluated using the NanoDrop 2000 spectrophotometer (Thermo Scientific, USA). RNA integrity was assessed using the Agilent 2100 Bioanalyzer (Agilent Technologies, USA). The samples with an RNA integrity number of ≥ 7 were processed for the subsequent analysis. Then the libraries were constructed using VAHTS Universal V6 RNA-seq Library Prep Kit (NR604-01, Vazyme) according to the manufacturer's instructions. The transcriptome sequencing and analysis were conducted by OE Biotech Co., Ltd. (Shanghai, China). The libraries were sequenced on an Illumina Novaseq 6000 platform and 150 bp paired-end reads were generated. About 55M raw reads for each sample were generated. Raw reads of FASTQ format were firstly processed using fastp and the low-quality reads were removed to obtain the clean reads. Then about 50M clean reads for each sample were retained for subsequent analyses. The clean reads were next mapped to the reference genome (mm10) using HISAT2 (26). Fragments per kb of transcript per million (FPKM) of each gene was calculated and the read counts of each gene were obtained by HTSeq-count (27).

Differential expression analysis was performed with DESeq2 (28). $Q < 0.05$ and fold change > 1.5 or < 0.67 was set as the threshold for significantly differential expression

gene (DEGs). Hierarchical clustering of DEGs was conducted in R (v 3.2.0) to visualize the expression patterns among groups and samples. GO and KEGG pathway enrichment analyses were conducted based on the hypergeometric distribution to identify significantly enriched terms. GSEA was conducted using the GSEA software (version 4.3.0) on the rank-ordered gene list, calculating enrichment scores and assessing statistical significance via permutation testing.

Metabolomics analysis

Hepa1-6 cells alone or activated CD8⁺ T cells and Hepa1-6 cells (5:1) were cultured for 48 hours. Then cell culture supernatant was collected, snap-frozen in liquid nitrogen and stored at -80°C. Subsequently, Tof-MRM (TM) widely-targeted metabolomics was performed by MetWare Biotechnology Co., Ltd (Wuhan, China) based on a previously described protocol (29). Further analysis, including PCA, volcano plot visualization and KEGG was conducted utilizing an online platform accessible at the following website: <https://cloud.metware.cn/>.

ELISA

Commercial ELISA kits were used for detection of PGE2 and murine IL-2, IFN- γ (EK8103, EK202, EK280 Multi Sciences) in serum and tumor-derived supernatant. For the detection of cytokines derived from TAMs and tumor-infiltrating NK cells, LEGENDplex (740446, 74051, Biolegend) and ELISA kits (SEB132Mu, SEA040Mu, Cloud clone; SP13754, SpBio) were utilized according to manufacturer's instructions.

Immunofluorescence and immunohistochemistry

FFPE sections (5 μ m) of murine or human tumor samples underwent de-paraffined

and rehydrated. Then antigen retrieval was performed utilizing EDTA antigen retrieval solution (C1034, Solarbio LIFE SCIENCE) at 95 °C for 20 minutes. Upon returning to room temperature, the sections were subsequently blocked with normal goat serum (ZLI-9056, ZSGB-BIO) at 37°C for a period of 1 hour. The sections were then incubated overnight at 4°C with the desired primary antibodies. The next day, to remove unbound antibodies, the slides were washed three times with Tris-Buffered Saline with Tween-20 (TBST, T1081, Solarbio LIFE SCIENCE).

For IF, fluorescent secondary antibodies were added and incubated in the dark at room temperature for 1 hour, and then washed three times with TBST. If tissue apoptosis needs to be detected, the slides were further stained using the TUNEL Apoptosis Detection Kit (40306ES50, Yeasen Biotechnology) according to the manufacturer's protocols. Nuclei were counterstained with DAPI (P0131, Beyotime) for 10 minutes at room temperature.

For IHC, the slides underwent additional blocking steps to inhibit endogenous horseradish peroxidase (HRP) and alkaline phosphatase (AP) activity using a specific blocking solution (R37629, Invitrogen). Following this, HRP- and AP-labeled secondary antibodies were applied and incubated at 37°C for 30 minutes. After three washes with TBST, the sections were sequentially visualized using DAB (34002, Thermo Scientific) and Vector blue (SK-5300, Vector laboratories) stains. Cover slips were mounted onto the slides using a glycerinated gelatin mounting medium (S2150, Solarbio LIFE SCIENCE).

IF slides were scanned using Panoramic SCAN 150 version 2.5 (3DHISTECH,

Hungary). The digital slides were then analyzed in CaseViewer version 2.4 (3DHISTECH, Hungary) software and captured representative 20×, 40× or 63× images. IHC slides were scanned using Olympus VS200 ASW version 3.2.1 (Olympus, Japan). The digital slides were then analyzed in Olympus OlyVIA version 3.1 software (Olympus, Japan) and captured representative 20× and 40× images. For IHC staining of patient tumor tissues, we evaluated five randomly selected 40× fields per slide for the presence of CX3CR1/CD68 double-positive cells. The mean count of these cells was considered as the number of CX3CR1⁺ TAM infiltration in tumor tissues. Patients were then stratified based on their CX3CR1⁺ TAM infiltration levels: those in the top 50% (≥ 5 in the 40× field) were categorized as the high infiltration group, while those in the bottom 50% (< 5 in the 40× field) were categorized as the low infiltration group. All primary and secondary antibodies used for IF/IHC are listed in Supplementary Table S2.

Western blot

Control Hepa1-6 cells or Hepa1-6 cells after immune attack experiments (see *In vitro primary cell experiments*) were lysed on ice using RIPA buffer (FD009, Fdbio science) with phosphatase inhibitor and protease inhibitor (FD1002, FD1001, Fdbio science). Subsequently, the lysates were then centrifuged at 12,000 rpm for 20 minutes and the supernatants were collected and the protein content quantified using the Pierce BCA Protein Assay Kit (23225, Thermo Scientific). A quantity of 20–40 ng of protein per sample were run on SurePAGE Bis-Tris gels (10% polyacrylamide, GenScript) and transferred on polyvinylidene difluoride (PVDF) membrane (Millipore). The PVDF

membranes were blocked by 5% BSA for 1 hour at room temperature. Then, the membranes were incubated overnight at 4 °C with the primary antibodies. After washing, the membranes were incubated with HRP-conjugated secondary antibody for 1 hour at room temperature. Staining was visualized by ECL kit (FD8000, Fdbio science) and acquired with the FluorChem E System (92-14860-00, ProteinSimple). All primary and secondary antibodies used for western blot are listed in Supplementary Table S2.

Quantitative PCR

Total RNA was extracted from 10^6 control Hepa1-6 cells or Hepa1-6 cells after immune attack experiments (see *In vitro primary cell experiments*) using RNeasy Mini Kit (74104, Qiagen), following the manufacturer's instructions. Subsequently, 1-2 µg of RNA was reverse transcribed into cDNA using the HiScript IV All-in-One Ultra RT SuperMix for qPCR (R433-01, Vazyme). Quantitative PCR was performed using the ChamQ SYBR qPCR Master Mix (Q311-02, Vazyme) with detection on a QuantStudio6 (Applied Biosystems) cycler with gene specific primers (Supplementary Table S3). At least three biological replicates were conducted for each experiment. The relative transcription levels were normalized to *Gapdh* expression levels using the $\Delta\Delta C_t$ method.

Bioinformatic analysis

To evaluate the TME characteristics in HCC patients following anti-PD-1 therapy, we harnessed publicly available bulk RNA sequencing (RNA-seq) datasets, specifically GSE202069 and ERP117672 (30,31). GSE202069 contained 66 patient-derived HCC

tissue or adjacent normal tissue gene expression profiles (mRNA expression matrix), and we selected gene expression profiles from all 17 tumor tissues that had been treated with anti-PD-1 therapy, with available clinical response. Similarly, ERP117672 included 128 patient-derived HCC tissue or adjacent normal tissue gene expression profiles (raw data in FASTQ format). We selected gene expression profiles from all 40 tumor tissues received anti-PD-1 therapy, with available clinical response. We implemented the R package "Combat" to mitigate batch effects and calculated feature scores through single-sample GSEA (ssGSEA), referencing gene sets from STRING, TISIDB, and the IOBR (32-35). Subsequently, we utilized the R package "Complexheatmap" to generate heatmaps, visually depicting the TME features and patient characteristics(36).

We assessed the correlation between the CX3CR1⁺ TAM-related signature and T-cell exhaustion using multiple datasets: TCGA-LIHC, GSE1898, and GSE54236 (37-39). The TCGA-LIHC dataset provided gene expression profiles for 366 patient HCC tissues and 50 normal tissues (mRNA expression matrix). GSE1898 contained gene expression profiles for tumor tissues from 91 HCC patients (mRNA expression matrix). GSE54236 included gene expression profiles for 81 patient HCC tissues and 80 normal tissues (mRNA expression matrix). We utilized the tumor tissue data from these datasets for further analysis. T-cell exhaustion scores were calculated using the Tumor Immune Dysfunction and Exclusion (TIDE) algorithm, and their correlation with the CX3CR1⁺ TAM-related signature was analyzed (40).

Additionally, to explore the prognostic significance of *Cx3cr1* and *Ptgs2* dual-gene

signature in HCC patients receiving anti-PD-1 therapy, we analyzed the GSE140901 dataset, which contained mRNA expression profiles of tumor tissues from 22 HCC patients who underwent anti-PD-1 therapy (41). Survival curves were generated on the Kaplan-Meier plotter website with auto best cut-off setting (42).

Statistical analysis

All statistical analyses were performed using Prism V.9 (GraphPad, USA). Unpaired two-tailed *t* test, Tukey multiple comparisons test and two-way ANOVA test were used for comparisons of normally distributed datasets. For survival analysis, *P* values were computed using the log-rank test. *P* value <0.05 were considered significant. *, *P* < 0.05; **, *P* < 0.01; ***, *P* < 0.001; ****, *P* < 0.0001; ns, not significant.

Data availability

The raw and processed high-throughput sequencing data have been deposited in the Gene Expression Omnibus (GEO) under accession numbers GSE232023, GSE232024 and GSE263240. All other data associated with this study are present in the main paper or the Supplementary Materials or are available from the corresponding author upon reasonable request.

Results

Anti-PD-1 therapy shows suboptimal efficacy in HCC

We evaluated the efficacy of anti-PD-1 therapy in an orthotopic Hepa1-6 HCC model. Through *in vivo* luciferase imaging and tumor size measurement, we observed a reduction in tumor size following anti-PD-1 treatment (Fig. 1A-C). However, we also noticed that although the tumor growth rate slowed down, the overall trend still showed a sustained growth (Fig. 1A-C). Initially, the anti-PD-1 therapy elicited an enhanced antitumor response, characterized by an increase in infiltrating cytotoxic CD8⁺ T cells and elevation in immune-supportive cytokines within the tumor tissues (Fig. 1D-F). Given that, the upregulation of inhibitory immune checkpoint molecules is a pivotal feature of CD8⁺ T-cell dysfunction in tumors, we examined the expression of several common immune checkpoint molecules, including lymphocyte activation gene-3 (LAG-3), T cell immunoglobulin and mucin domain-3 (TIM-3), T cell immunoreceptor with Ig and ITIM domains (TIGIT), and PD-1, on tumor-infiltrating CD8⁺ T cells. Our results demonstrated a moderate, but not significant, increase in LAG-3 and PD-1 expression during the treatment. However, in the anti-PD-1 treatment group, TIM-3 expression was significantly upregulated in CD8⁺ T cells compared to the IgG treatment (Fig. 1G-I). A pattern consistent with these data was observed in the H22 orthotopic HCC model (Supplementary Fig. S2).

Collectively, these findings suggest that TIM-3, an indicator of CD8⁺ T-cell dysfunction, may serve as a compensatory mechanism in HCC, limiting the efficacy of anti-PD-1 therapy.

CX3CR1⁺ TAMs accumulate in HCC upon anti-PD-1 treatment

While analyzing lymphocytes in tumor tissue, we also analyzed the dynamic changes of other immune cell subsets, especially tumor-infiltrating myeloid cells, during anti-PD-1 therapy. On day 4, neutrophils constituted over 30% of the CD45⁺ tumor-infiltrating immune cells, but their proportion declined over time, with a corresponding increase in monocytes and dendritic cells (Fig. 2A-C). Furthermore, TAMs accumulated rapidly in the anti-PD-1 treatment group, comprising 23.6% of total tumor-infiltrating immune cells by day 14, contrasting with 12.3% in the IgG-treated group (Fig. 2D). Phenotype analysis of TAMs showed distinct surface marker expression pattern. Despite the transient elevation of MHC II expression on day 7 following anti-PD-1 treatment, no significant difference in MCH II levels were seen between the two groups from day 10 on (Fig. 2E). In contrast, the expression of CX3CR1, another inflammatory marker, was significantly upregulated in anti-PD-1-treated tumors throughout the time course of the experiment (Fig. 2F-G). To elucidate the transcriptional features of CX3CR1⁺ TAMs, we conducted scRNA-seq on sorted CD45⁺ tumor-infiltrating immune cells. Differential gene expression analysis between CX3CR1⁺ (*Csf1r*⁺*Cd68*⁺*Itgam*⁺*Cx3cr1*⁺) and CX3CR1⁻ (*Csf1r*⁺*Cd68*⁺*Itgam*⁺*Cx3cr1*⁻) TAMs revealed key insights (Fig. 2H). KEGG pathway analysis demonstrated a significant upregulation of ER protein processing, HIF-1 α signaling, and glycolysis in CX3CR1⁺ TAMs, indicative of an active metabolic state (Fig. 2I). Conversely, these cells exhibited reduction in oxidative phosphorylation and ROS generation pathways compared to CX3CR1⁻ TAMs (Fig. 2J). In addition,

CX3CR1⁺ TAMs in anti-PD-1-treated tumors displayed enrichment in antigen presentation, cytokine signaling, and other adaptive immune system-related pathways, compared with IgG-treated tumors (Fig. 2K). These findings suggest that CX3CR1⁺ TAMs possess an active metabolic profile and cytokine production capacity, potentially linked to adaptive immune responses.

Blocking CX3CR1 enhances the efficacy of anti-PD-1 therapy

To explore whether inhibiting CX3CR1⁺ TAMs can enhance the therapeutic effect of anti-PD-1 therapy, we treated Hepa1-6 orthotopic tumor-bearing mice with CX3CR1 neutralizing antibodies and/or anti-PD-1. Our findings indicated a profound effect of the combination therapy on tumor progression, demonstrated by a substantial reduction in tumor size and a significant improvement in survival rates (Fig. 3A-C).

Furthermore, we analyzed the influence of anti-CX3CR1 therapy on the immune landscape within the TME. Our results demonstrate that CX3CR1 neutralization led to a notable decrease in TAM infiltration, accompanied by an increased proportion of CD8⁺ T cells (Fig. 3D). Tumors treated with the combination therapy exhibited a significant increase in activated CD8⁺ T cells compared to control or monotherapy groups (Fig. 3E). Moreover, CX3CR1 neutralizing antibodies mitigated the upregulation of TIM-3, indicating a potential attenuation of T-cell exhaustion (Fig. 3F). Additionally, we observed a reduction in the percentage of CX3CR1⁺ subpopulations among TAMs (Fig. 3G-H).

To further investigate the effect of CX3CR1 neutralization on TAMs, we conducted a series of *in vivo* and *in vitro* experiments. Our findings indicate that CX3CR1

neutralization in the Hepa1-6 orthotopic model significantly reduced the survival of TAMs and increased their apoptosis rate (Fig. 3I-K). Similar trend was observed in *in vitro* experiments with BMDMs. The use of CX3CR1-specific antibody significantly reduced the proportion of proliferative marker Ki-67 in BMDMs, and increased the proportion of apoptotic marker Annexin V. Conversely, CX3CR1 overexpression in BMDMs significantly elevated Ki-67 levels and reduced Annexin V levels. Notably, CX3CR1 effectively reversed these effects, indicating a critical role for CX3CR1 in modulating BMDM proliferation and apoptosis (Fig. 3L-M). Furthermore, CX3CR1 inhibition exerted a profound transcriptional impact on TAMs in the Hepa1-6 orthotopic model, substantially augmenting the TNF signaling pathway while suppressing arachidonic acid metabolism, cholesterol metabolism, and the PPAR signaling pathway, in contrast to IgG therapy (Supplementary Fig. S3A). Moreover, when compared to anti-PD-1 monotherapy, combination therapy further amplified TNF and IL-17 signaling in TAMs while inhibiting the PD-L1 pathway, arachidonic acid metabolism, and PPAR signaling (Supplementary Fig. S3B). We further explored the effect of CX3CR1 neutralization on TAM recruitment. In transwell assays with different chemoattractants including serum-free DMEM, Hepa1-6 tumor supernatant, and Hepa1-6 tumor supernatant +10 $\mu\text{g}/\text{mL}$ CX3CR1-specific antibody, neither CX3CR1 overexpression nor neutralization affected the chemotaxis of BMDMs (Supplementary Fig. S3C). Similarly, in ACT experiments, no remarkable difference in macrophage enrichment was observed between CX3CR1-overexpression and neutralization groups (Supplementary Fig. S3D). Analysis of common chemokines

revealed that levels of CCL2, CCL3, CCL4, and CXCL1 in Hepa1-6-luci tumor tissues were markedly higher than those of CX3CL1, suggesting a less pronounced chemotaxis role for CX3CL1 (Supplementary Fig. S3E). In addition, CX3CR1 flow staining suggested that the observed neutralizing effect was not influenced by antigen masking factors (Supplementary Fig. S3F).

Given the significant upregulation of TIM-3 on CD8⁺ T cells in the anti-PD-1 treatment group, we included anti-TIM-3 and anti-TIM-3/anti-PD-1 combination treatment in the same batch of our animal experiments (anti-CX3CR1/anti-PD-1). Our results showed that anti-TIM-3 significantly enhanced the effectiveness of anti-PD-1 therapy, resulting in a substantial tumor reduction (Supplementary Fig. S4A-B), consistent with previous reports (43,44).

Although NK-cell and NKT-cell populations constitute relatively small components in our orthotopic Hepa1-6 HCC model, we evaluated their functional status, particularly their activation marker CD69 and cytokine secretion under different immunotherapy combinations. Our analysis showed that different treatment combinations had no significant impact on these cells (Supplementary Fig. S4C-I).

IL-27 derived from CX3CR1⁺ TAMs promotes CD8⁺ T-cell exhaustion

To investigate the regulatory role of CX3CR1⁺ TAMs in anti-PD-1 therapy, we isolated CX3CR1⁺ and CX3CR1⁻ TAMs from anti-PD-1 treated tumors for *in vitro* analysis (Fig. 4A). Cytokine profiling analyses demonstrated significantly elevated IL-27 levels in the supernatant derived from CX3CR1⁺ TAMs (Fig. 4B). When CX3CR1⁺ TAMs were co-cultured with CD8⁺ T cells, we observed an upregulation of

TIM-3 expression on CD8⁺ T cells (Fig. 4C). This upregulation was accompanied by a reduction in the production of functional cytokines, such as TNF- α and IFN- γ , while the proliferation of the CD8⁺ T cells remained largely unchanged (Fig. 4D, Supplementary Fig. S5A-B). TIM-3 expression was significantly upregulated on proliferating T cells (Supplementary Fig. S5C). Furthermore, our experiments revealed that the inhibitory effect of CX3CR1⁺ TAMs on CD8⁺ T cells was simulated by exogenous IL-27 addition and abrogated by IL-27 neutralization, indicating a role for IL-27 in mediating CX3CR1⁺ TAM-induced T-cell exhaustion (Fig. 4C-D).

To gain further insights into the role of CX3CR1⁺ TAMs in inducing T-cell exhaustion *in vivo*, we employed a macrophage-tumor Winn assay (Fig. 4E). Our findings indicate that overexpression of CX3CR1 in BMDMs (CX3CR1^{OE} M ϕ) significantly enhanced IL-27 secretion and upregulated CD86 expression, thereby partially recapitulating the phenotypic characteristics of CX3CR1⁺ TAMs (Supplementary Fig. S5D-G). When co-injected with tumor cells into mice, CX3CR1^{OE} M ϕ markedly accelerated tumor growth compared to Ctrl M ϕ (Fig. 4F-G), indicating that the TME is likely more immunosuppressive in the presence of CX3CR1^{OE} M ϕ . Consistent with this, further analysis of the TME revealed a reduction in the frequencies of T cells and NK cells, while myeloid cells, particularly TAMs, were significantly increased (Fig. 4H). These TAMs exhibited upregulated expression of CX3CR1 and Ki-67 (Fig. 4I). Further analysis of the tumor-infiltrating CD8⁺ T cells revealed upregulation of PD-1 and TIM-3, accompanied by downregulation of functional marker CD107a and activation marker CD69 (Fig. 4J-K). Additionally, the production of functional

cytokines, including IFN- γ and TNF- α , was significantly reduced in CD8⁺ T cells (Fig. 4L).

Collectively, our *in vitro* and *in vivo* assays demonstrate that IL-27 derived from CX3CR1⁺ TAMs has a potent capacity to induce CD8⁺ T-cell dysfunction. This suggests that IL-27-producing CX3CR1⁺ TAMs may contribute to the suboptimal efficacy of anti-PD-1 therapy.

Immune-attacked tumor cells release PGE2 to induce CX3CR1 upregulation in macrophages

Previous studies have demonstrated modulation of the macrophage phenotype by diverse factors (45). To explore the potential influence of these factors, we exposed BMDMs to a variety of differentiation conditions. Our results indicate that common stimuli, such as LPS/IFN- γ , IL-4/IL-13, and hypoxia, exhibited minimal effects on CX3CR1 expression (Fig. 5A). In contrast, we found that tumor supernatant alone induced a partial upregulation of CX3CR1, while tumor supernatant obtained following activated CD8⁺ T cell attack significantly augmented CX3CR1 expression on BMDMs (Fig. 5A, Supplementary Fig. S6A).

A growing body of evidence shows that the metabolic characteristics in TAMs are dynamic during their differentiation and activation (46,47). To identify metabolites potentially responsible for CX3CR1 upregulation, we conducted metabolomic analysis of supernatants derived from tumor cells with or without immune attack (Fig. 5B). Our analysis revealed a significant increase in PGE2 levels in the tumor supernatant following immune attack (Fig. 5C-E, Supplementary Fig. S6B).

Furthermore, transcriptomic analysis and immunoblotting of tumor cell pellets demonstrated an upregulation of arachidonic acid metabolic pathway and its key enzymes cyclooxygenase-2 (COX-2) and microsomal Prostaglandin E Synthase-1 (mPGES-1), following immune attack (Fig. 5F-G). These findings suggest that PGE2 plays a critical role in tumor metabolic remodeling in response to immune challenge, potentially influencing the immune landscape within the TME. Consistent with this, the addition of exogenous PGE2 simulated the effect of immune-attacked tumor supernatant, promoting the differentiation of BMDMs towards a CX3CR1⁺ phenotype (Fig. 5H, Supplementary Fig. S6C). Treatment of BMDMs with a prostaglandin receptor 4 (EP4) inhibitor abrogated the upregulation of CX3CR1, whereas an EP2 inhibitor did not have such an effect (Fig. 5I, Supplementary Fig. S6D). This indicates that PGE2 mediates the upregulation of CX3CR1 in BMDMs via EP4 interaction.

Collectively, our results demonstrated that PGE2 released by immune-attacked tumor cells drives the phenotypic transition of macrophages towards a CX3CR1⁺ phenotype.

Blocking COX-2 improves the efficacy of anti-PD-1 therapy

The above results elucidate a role for PGE2, derived from immune-attacked tumor cells, in modulating CX3CR1 expression in TAMs. Therefore, we further investigated the therapeutic potential of PGE2 inhibition during anti-PD-1 therapy. In the orthotopic Hepa1-6 HCC model, mice treated with a combination of anti-PD-1 and the COX-2 inhibitor Celecoxib (CXB) exhibited significant tumor growth suppression (Fig. 6A-C). Administration of CXB significantly reduced PGE2 levels in both peripheral blood and tumor tissues, while CX3CR1 inhibition had no significant effect

on PGE2 content in tumor tissues (Fig. 6D-E, Supplementary Fig. S6E). Furthermore, the proportion of CX3CR1⁺ TAM was significantly reduced in the CXB treatment group and the combination treatment group (Fig. 6F). Additionally, the proportion of CD8⁺ T cells expressing TIM-3 significantly decreased, while the expression levels of IFN- γ , TNF- α , and PRF significantly increased in combination treatment group (Fig. 6G-H). These results suggest that blocking PGE2 release during anti-PD-1 therapy can mitigate the transition of TAMs to an inhibitory CX3CR1⁺ phenotype and enhance anti-PD-1 therapy efficacy.

CX3CR1⁺ TAMs and elevated PGE2 suggest poor efficacy of anti-PD-1 therapy

Next, we aimed to assess the correlation between CX3CR1⁺ TAMs, its upstream PGE2 metabolic process and immunotherapy efficacy in HCC patients. Initially, we examined the infiltration of CX3CR1⁺ TAMs and preoperative serum PGE2 levels in patients undergoing neoadjuvant anti-PD-1 based immunotherapy (ICI Cohort #1, Supplementary Fig. S7A). Our results revealed a significant association between increased infiltration of CX3CR1⁺ TAMs and poorer RFS (log-rank $P = 0.0118$, Fig. 7A-B). Additionally, we observed that patients with stable disease (SD, no disease progression or recurrence within 6 months post-surgery) exhibited significantly lower preoperative serum PGE2 levels (Fig. 7C). Furthermore, patients with lower preoperative serum PGE2 levels exhibited significantly improved RFS (log rank $P = 0.0174$, Fig. 7D). We also collected serial peripheral blood samples from HCC patients undergoing anti-PD-1 therapy to monitor PGE2 levels (ICI Cohort #2, Supplementary Fig. 7B). Our analysis revealed that patients experiencing disease

progression (PD) within 6 months exhibited a gradual increase in serum PGE2. Conversely, patients achieving stable disease (SD) or partial response (PR) maintained relatively stable PGE2 levels throughout the treatment period (Fig. 7E). Finally, we further validated our findings using publicly available sequencing datasets. We integrated tumor tissue RNA-seq datasets of HCC patients treated with anti-PD-1 therapy (GSE202069, ERP117672) and calculated CX3CR1⁺ TAM-related gene signature scores and TME feature scores (Supplementary Fig. S7C). Specifically, we found that CX3CR1⁺ TAM-related gene signatures were enriched in HCC patients who did not respond to anti-PD-1 treatment and were closely associated with highly suppressive TME features, characterized by decreased levels of immune supportive cytokines, decreased immune infiltration, and higher expression of immune checkpoints (Fig. 7F-G). Through TIDE analysis, we also found that CX3CR1⁺ TAM-associated genes were closely related to T-cell exhaustion (Supplementary Fig. S7D). Furthermore, analysis of the “*Cx3cr1-Ptgs2*” dual signal in an HCC immunotherapy cohort (GSE140901) indicated that higher expression of these genes was associated with poor overall survival (OS) and progression-free survival (PFS) (log rank $P=0.027$ and 0.046 , respectively, Fig. 7H-I).

Overall, our results suggest a correlation between higher CX3CR1⁺ TAM infiltration, higher serum PGE2 level and suboptimal efficacy of anti-PD-1 therapy in HCC patients. This finding further underscores the significant role of CX3CR1⁺ TAM and PGE2 in limiting the efficacy of anti-PD-1 therapy in HCC.

Discussion

The discovery of immune checkpoint mechanisms and subsequent development of ICIs have revolutionized cancer treatment (48). Although ICIs have proven effective in multiple cancers, the response rate among HCC patients remains below 20% (7,8). One potential mechanism underlying this resistance is tumor immune escape facilitated by TAMs (49,50). TAMs constitute a substantial and heterogeneous immune component within the HCC TME. Their precise roles in the context of immunotherapy remain to be further elucidated.

In this study, we have demonstrated that PGE₂ released from HCC cells under immune attack educates TAMs, resulting in EP4-dependent upregulation of CX3CR1. Our findings further reveal that CX3CR1⁺ TAMs facilitate the dysfunction of tumor-infiltrating CD8⁺ T cells through the secretion of IL-27. Blocking CX3CR1 or the release of PGE₂ can significantly enhance the efficacy of anti-PD-1 therapy, reduce the proportion of CX3CR1⁺ TAMs, and alleviate CD8⁺ T-cell dysfunction. Based on these findings, arachidonic acid metabolism and CX3CR1⁺ TAM-related signatures may serve as potential markers for predicting the therapeutic response to anti-PD-1 in HCC patients. Furthermore, these molecules might represent viable targets for enhancing the efficacy of immunotherapy in HCC patients (Supplementary Fig. S7E).

In our preclinical study using murine HCC models, accumulation of TAMs was observed in anti-PD-1 therapy groups. Phenotypic analysis revealed a considerable upregulation of CX3CR1 expression in TAMs, a biomarker closely associated with inflammation and tumorigenesis (51). CX3CR1⁺ TAMs have been characterized in

recent studies as exhibiting a mixed phenotype, possessing both pro-inflammatory and anti-inflammatory properties (20). The ablation of these TAMs has been linked to favorable immunotherapy outcomes (19,20,52). In addition, in breast cancer patients with reduced response to ICI, CX3CR1⁺ TAMs tend to accumulate and inversely correlate with T cell expansion (21). Through transcriptomic analyses, we observed elevated expression of genes related to glycolytic metabolism, cytokine secretion, and antigen presentation. These findings suggest a close association between CX3CR1⁺ TAMs and the adaptive immune system, highlighting their potential role in shaping the immune response within the TME.

To explore the interplay between CX3CR1⁺ TAMs and CD8⁺ T cells, we conducted *in vitro* co-culture experiments and *in vivo* Winn assays. Our findings indicate that CX3CR1⁺ TAMs promote TIM-3 upregulation and dysfunction in CD8⁺ T cells via IL-27 secretion. Previous studies have also highlighted the negative effects of CX3CR1⁺ myeloid cells in inflammatory liver diseases and HCC (53-55), emphasizing the significance of CX3CR1⁺ TAMs and the potential of targeting CX3CR1 in tumor immunotherapy.

IL-27, a heterodimeric cytokine comprising the subunits EB13 and IL-27p28, belongs to the IL-6/IL-12 family and plays a pivotal role in orchestrating immune responses (56). Myeloid cells, including dendritic cells, monocytes, and macrophages are the primary producers of IL-27 (57). While IL-27 has been known for its immune-activating effects (58,59), recent studies have revealed its potential negative impact on antitumor immunity. For instance, IL-27 has been shown to promote the

expression of CD39 in tumor-infiltrating Tregs, enhance the expression of multiple coinhibitory receptors, and facilitate the expansion of IL-10-producing type 1 regulatory T cells (Tr1) (60,61). In HCC, elevated serum IL-27 levels are significantly associated with an increased risk of HCC development, and blocking IL-27R improves the efficacy of immunotherapy in preclinical models (62,63). Consistent with previous studies (64), our study suggests that tumor infiltrating CX3CR1⁺ TAMs are a rich source of IL-27, and IL-27 plays an important role in mediating CD8⁺ T-cell dysfunction. These findings emphasize their crucial role in HCC TME.

Macrophages' functional characteristics are profoundly influenced by diverse microenvironmental factors (65). Recent studies have underscored the importance of the metabolic profile of the TME in shaping the phenotype of TAMs. For instance, in renal cancer, the augmented glutamate consumption by cancer cells prompts TAMs to produce IL-23, thereby facilitating tumor immune evasion (47). Similarly, in melanoma, high histamine levels upregulate the immune checkpoint VISTA in TAMs, leading to T-cell exhaustion (66,67). Our study demonstrates that HCC exhibit elevated levels of PGE2 during immune attacks triggered by CTLs *in vitro* or in response to anti-PD-1 therapy *in vivo*. This aligns with Fotis et al., who showed that PGE2 released by dying tumor cells acts as an inhibitory damage-associated molecular pattern (DAMP), compromising immunotherapy efficacy in bladder cancer (68). However, our study uncovered a distinct mechanism where PGE2 promotes the transition to a CX3CR1⁺ phenotype, which can induce T-cell exhaustion. The divergent outcomes observed in our study compared to those reported by Fotis et al.

highlight the plasticity and context- dependency of the PGE2 signaling within the TME. These differences may be attributed to distinct metabolic and immunological profiles among tumor types, thereby modulating the downstream effects of PGE2 on TAM polarization and immune responses.

Non-steroidal anti-inflammatory drugs (NSAIDs), are well-known for their protective effects in cancer patients by blocking COX activity and prostaglandin biosynthesis (68,69). Our findings revealed a correlation between high serum PGE2 levels, high CX3CR1⁺ TAM infiltration and a poor immunotherapy response in HCC patients. This suggests that PGE2 and CX3CR1⁺ TAMs may limit the efficacy of HCC immunotherapy. Based on these findings, targeting CX3CR1⁺ TAMs and blockade of PGE2 release may serve as potential strategies to enhance the efficacy of anti-PD-1 therapy in HCC.

There are several limitations in our study. First, as the diagnosis of HCC primarily relies on imaging evidence, biopsy samples before immunotherapy are scarce, which makes it difficult for us to conduct a detailed analysis of the TME at the treatment baseline. Second, the prescription preferences of doctors and the difficulty in tracking NSAID uses make it difficult to directly evaluate the specific effects of NSAIDs on HCC immunotherapy. To address these issues, future research needs to conduct larger scale, multicenter clinical trials, as well as prospective clinical cohort studies, to evaluate the potential advantages and limitations of combining NSAIDs with immunotherapy in the treatment of HCC.

In summary, this study demonstrates that CX3CR1⁺ TAMs limits anti-PD-1 therapy in

HCC. Combining CX3CR1 neutralizing antibody with anti-PD-1 effectively inhibited HCC growth, reduced CX3CR1⁺ TAM infiltration, and restored CD8⁺ T-cell function. PGE2 release from immune-attacked tumor cells drove TAMs to a CX3CR1⁺ phenotype. Taken together, blocking CX3CR1⁺ TAMs and PGE2 release are promising strategies to enhance current anti-PD-1 therapy in HCC.

Author's Contributions

X. Xiang: Conceptualization, investigation, visualization, methodology, writing—original draft. **K. Wang:** Conceptualization, formal analysis, writing—review and editing. **H. Zhang:** Conceptualization, investigation, methodology. **H. Mou:** Validation, formal analysis. **Z. Shi:** Investigation, methodology. **Y. Tao:** Investigation, methodology. **H. Song:** Investigation, methodology. **Z. Lian:** Investigation, methodology. **S. Wang:** Formal analysis, visualization. **D. Lu:** Formal analysis, visualization. **X. Wei:** Resources. **H. Xie:** Resources. **S. Zheng:** Resources. **J. Wang:** Conceptualization, supervision, writing—review and editing. **X. Xu:** Conceptualization, supervision, writing—review and editing, Funding acquisition.

Acknowledgements

We are grateful to Prof. Kouros Saeb-Parsy and Dr. Matthew Hoare from University of Cambridge for their invaluable advice on this work. We also thank Dr. Jian Chen from University of Cambridge and Dr. Rui Wang from Zhejiang University School of Medicine, for their support in bioinformatics data processing and analyzing.

References

1. Sung H, Ferlay J, Siegel RL, Laversanne M, Soerjomataram I, Jemal A, *et al.* Global Cancer Statistics 2020: GLOBOCAN Estimates of Incidence and Mortality Worldwide for 36 Cancers in 185 Countries. *CA Cancer J Clin* **2021**;71(3):209-49 doi 10.3322/caac.21660.
2. Vogel A, Meyer T, Sapisochin G, Salem R, Saborowski A. Hepatocellular carcinoma. *The Lancet* **2022** doi 10.1016/s0140-6736(22)01200-4.
3. Gunasekaran G, Bekki Y, Lourdasamy V, Schwartz M. Surgical Treatments of Hepatobiliary Cancers. *Hepatology* **2020** doi 10.1002/hep.31325.
4. Cheng A-L, Hsu C, Chan SL, Choo S-P, Kudo M. Challenges of combination therapy with immune checkpoint inhibitors for hepatocellular carcinoma. *Journal of Hepatology* **2020**;72(2):307-19 doi 10.1016/j.jhep.2019.09.025.
5. Zhang Y, Zhang Z. The history and advances in cancer immunotherapy: understanding the characteristics of tumor-infiltrating immune cells and their therapeutic implications. *Cell Mol Immunol* **2020**;17(8):807-21 doi 10.1038/s41423-020-0488-6.
6. Wei SC, Duffy CR, Allison JP. Fundamental Mechanisms of Immune Checkpoint Blockade Therapy. *Cancer Discov* **2018**;8(9):1069-86 doi 10.1158/2159-8290.CD-18-0367.
7. El-Khoueiry AB, Sangro B, Yau T, Crocenzi TS, Kudo M, Hsu C, *et al.* Nivolumab in patients with advanced hepatocellular carcinoma (CheckMate 040): an open-label, non-comparative, phase 1/2 dose escalation and expansion trial. *The Lancet* **2017**;389(10088):2492-502 doi 10.1016/s0140-6736(17)31046-2.
8. Zhu AX, Finn RS, Edeline J, Cattan S, Ogasawara S, Palmer D, *et al.* Pembrolizumab in patients with advanced hepatocellular carcinoma previously treated with sorafenib (KEYNOTE-224): a non-randomised, open-label phase 2 trial. *The Lancet Oncology* **2018**;19(7):940-52 doi 10.1016/s1470-2045(18)30351-6.
9. Aldea M, Andre F, Marabelle A, Dogan S, Barlesi F, Soria JC. Overcoming Resistance to Tumor-Targeted and Immune-Targeted Therapies. *Cancer Discov* **2021**;11(4):874-99 doi 10.1158/2159-8290.CD-20-1638.
10. Xiang X, Wang J, Lu D, Xu X. Targeting tumor-associated macrophages to synergize tumor immunotherapy. *Signal Transduct Target Ther* **2021**;6(1):75 doi 10.1038/s41392-021-00484-9.
11. O'Rourke JM, Patten DA, Shetty S. Tumour-associated macrophages in hepatocellular carcinoma: Pressing the metabolic switch to prevent T cell responses. *J Hepatol* **2019**;71(2):243-5 doi 10.1016/j.jhep.2019.05.019.
12. Wu Q, Zhou W, Yin S, Zhou Y, Chen T, Qian J, *et al.* Blocking Triggering Receptor Expressed on Myeloid Cells-1-Positive Tumor-Associated Macrophages Induced by Hypoxia Reverses Immunosuppression and Anti-Programmed Cell Death Ligand 1 Resistance in Liver Cancer. *Hepatology* **2019**;70(1):198-214 doi 10.1002/hep.30593.
13. Chen DP, Ning WR, Jiang ZZ, Peng ZP, Zhu LY, Zhuang SM, *et al.* Glycolytic activation of peritumoral monocytes fosters immune privilege via the PFKFB3-PD-L1 axis in human hepatocellular carcinoma. *J Hepatol* **2019**;71(2):333-43 doi 10.1016/j.jhep.2019.04.007.
14. Rivas-Fuentes S, Salgado-Aguayo A, Arratia-Quijada J, Gorocica-Rosete P. Regulation and biological functions of the CX3CL1-CX3CR1 axis and its relevance in solid cancer: A mini-review. *J Cancer* **2021**;12(2):571-83 doi 10.7150/jca.47022.
15. Schmall A, Al-Tamari HM, Herold S, Kampschulte M, Weigert A, Wietelmann A, *et al.*

- Macrophage and cancer cell cross-talk via CCR2 and CX3CR1 is a fundamental mechanism driving lung cancer. *Am J Respir Crit Care Med* **2015**;191(4):437-47 doi 10.1164/rccm.201406-1137OC.
16. Jung K, Heishi T, Khan OF, Kowalski PS, Incio J, Rahbari NN, *et al.* Ly6Clo monocytes drive immunosuppression and confer resistance to anti-VEGFR2 cancer therapy. *J Clin Invest* **2017**;127(8):3039-51 doi 10.1172/JCI93182.
 17. Zheng J, Yang M, Shao J, Miao Y, Han J, Du J. Chemokine receptor CX3CR1 contributes to macrophage survival in tumor metastasis. *Mol Cancer* **2013**;12(1):141 doi 10.1186/1476-4598-12-141.
 18. Guldner IH, Wang Q, Yang L, Golomb SM, Zhao Z, Lopez JA, *et al.* CNS-Native Myeloid Cells Drive Immune Suppression in the Brain Metastatic Niche through Cxcl10. *Cell* **2020** doi 10.1016/j.cell.2020.09.064.
 19. Gubin MM, Esaulova E, Ward JP, Malkova ON, Runci D, Wong P, *et al.* High-Dimensional Analysis Delineates Myeloid and Lymphoid Compartment Remodeling during Successful Immune-Checkpoint Cancer Therapy. *Cell* **2018**;175(4):1014-30 e19 doi 10.1016/j.cell.2018.09.030.
 20. Jackaman C, Yeoh TL, Acuil ML, Gardner JK, Nelson DJ. Murine mesothelioma induces locally-proliferating IL-10(+)TNF-alpha(+)CD206(-)CX3CR1(+) M3 macrophages that can be selectively depleted by chemotherapy or immunotherapy. *Oncoimmunology* **2016**;5(6):e1173299 doi 10.1080/2162402X.2016.1173299.
 21. Bassez A, Vos H, Van Dyck L, Floris G, Arijs I, Desmedt C, *et al.* A single-cell map of intratumoral changes during anti-PD1 treatment of patients with breast cancer. *Nat Med* **2021**;27(5):820-32 doi 10.1038/s41591-021-01323-8.
 22. Seymour L, Bogaerts J, Perrone A, Ford R, Schwartz LH, Mandrekas S, *et al.* iRECIST: guidelines for response criteria for use in trials testing immunotherapeutics. *The Lancet Oncology* **2017**;18(3):e143-e52 doi 10.1016/s1470-2045(17)30074-8.
 23. Chen S, Zhou Y, Chen Y, Gu J. fastp: an ultra-fast all-in-one FASTQ preprocessor. *Bioinformatics (Oxford, England)* **2018**;34(17):i884-i90 doi 10.1093/bioinformatics/bty560.
 24. Zhang X, Lan Y, Xu J, Quan F, Zhao E, Deng C, *et al.* CellMarker: a manually curated resource of cell markers in human and mouse. *Nucleic acids research* **2019**;47(D1):D721-d8 doi 10.1093/nar/gky900.
 25. Aran D, Looney AP, Liu L, Wu E, Fong V, Hsu A, *et al.* Reference-based analysis of lung single-cell sequencing reveals a transitional profibrotic macrophage. *Nat Immunol* **2019**;20(2):163-72 doi 10.1038/s41590-018-0276-y.
 26. Kim D, Langmead B, Salzberg SL. HISAT: a fast spliced aligner with low memory requirements. *Nature methods* **2015**;12(4):357-60 doi 10.1038/nmeth.3317.
 27. Anders S, Pyl PT, Huber W. HTSeq--a Python framework to work with high-throughput sequencing data. *Bioinformatics (Oxford, England)* **2015**;31(2):166-9 doi 10.1093/bioinformatics/btu638.
 28. Love MI, Huber W, Anders S. Moderated estimation of fold change and dispersion for RNA-seq data with DESeq2. *Genome biology* **2014**;15(12):550 doi 10.1186/s13059-014-0550-8.
 29. Gong L, Zhang Y, Zhao J, Zhang Y, Tu K, Jiao L, *et al.* All-In-One Biomimetic Nanoplatform Based on Hollow Polydopamine Nanoparticles for Synergistically Enhanced Radiotherapy of

- Colon Cancer. Small (Weinheim an der Bergstrasse, Germany) **2022**;18(14):e2107656 doi 10.1002/sml.202107656.
30. Li B, Cao Y, Li Y, Cheng C, Yu D. Letter to the editor: the inflamed subclass predicts immunotherapy response - external validations. *Gut* **2022** doi 10.1136/gutjnl-2022-328130.
 31. Hong JY, Cho HJ, Sa JK, Liu X, Ha SY, Lee T, *et al.* Hepatocellular carcinoma patients with high circulating cytotoxic T cells and intra-tumoral immune signature benefit from pembrolizumab: results from a single-arm phase 2 trial. *Genome medicine* **2022**;14(1):1 doi 10.1186/s13073-021-00995-8.
 32. Zhang Y, Parmigiani G, Johnson WE. ComBat-seq: batch effect adjustment for RNA-seq count data. *NAR Genomics and Bioinformatics* **2020**;2(3) doi 10.1093/nargab/lqaa078.
 33. Ru B, Wong CN, Tong Y, Zhong JY, Zhong SSW, Wu WC, *et al.* TISIDB: an integrated repository portal for tumor-immune system interactions. *Bioinformatics* **2019**;35(20):4200-2 doi 10.1093/bioinformatics/btz210.
 34. Szklarczyk D, Kirsch R, Koutrouli M, Nastou K, Mehryary F, Hachilif R, *et al.* The STRING database in 2023: protein-protein association networks and functional enrichment analyses for any sequenced genome of interest. *Nucleic Acids Res* **2023**;51(D1):D638-d46 doi 10.1093/nar/gkac1000.
 35. Zeng D, Ye Z, Shen R, Yu G, Wu J, Xiong Y, *et al.* IOBR: Multi-Omics Immuno-Oncology Biological Research to Decode Tumor Microenvironment and Signatures. *Frontiers in Immunology* **2021**;12 doi 10.3389/fimmu.2021.687975.
 36. Gu Z, Eils R, Schlesner M. Complex heatmaps reveal patterns and correlations in multidimensional genomic data. *Bioinformatics* **2016**;32(18):2847-9 doi 10.1093/bioinformatics/btw313.
 37. Cancer Genome Atlas Research Network. Electronic address wbe, Cancer Genome Atlas Research N. Comprehensive and Integrative Genomic Characterization of Hepatocellular Carcinoma. *Cell* **2017**;169(7):1327-41 e23 doi 10.1016/j.cell.2017.05.046.
 38. Lee JS, Chu IS, Mikaelyan A, Calvisi DF, Heo J, Reddy JK, *et al.* Application of comparative functional genomics to identify best-fit mouse models to study human cancer. *Nature genetics* **2004**;36(12):1306-11 doi 10.1038/ng1481.
 39. Villa E, Critelli R, Lei B, Marzocchi G, Cammà C, Giannelli G, *et al.* Neoangiogenesis-related genes are hallmarks of fast-growing hepatocellular carcinomas and worst survival. Results from a prospective study. *Gut* **2016**;65(5):861-9 doi 10.1136/gutjnl-2014-308483.
 40. Jiang P, Gu S, Pan D, Fu J, Sahu A, Hu X, *et al.* Signatures of T cell dysfunction and exclusion predict cancer immunotherapy response. *Nat Med* **2018**;24(10):1550-8 doi 10.1038/s41591-018-0136-1.
 41. Hsu C-L, Ou D-L, Bai L-Y, Chen C-W, Lin L, Huang S-F, *et al.* Exploring Markers of Exhausted CD8 T Cells to Predict Response to Immune Checkpoint Inhibitor Therapy for Hepatocellular Carcinoma. *Liver Cancer* **2021**;10(4):346-59 doi 10.1159/000515305.
 42. Kovács SA, Fekete JT, Györfy B. Predictive biomarkers of immunotherapy response with pharmacological applications in solid tumors. *Acta pharmacologica Sinica* **2023**;44(9):1879-89 doi 10.1038/s41401-023-01079-6.
 43. Liu F, Liu Y, Chen Z. Tim-3 expression and its role in hepatocellular carcinoma. *J Hematol Oncol* **2018**;11(1):126 doi 10.1186/s13045-018-0667-4.
 44. Kim HD, Song GW, Park S, Jung MK, Kim MH, Kang HJ, *et al.* Association Between

- Expression Level of PD1 by Tumor-Infiltrating CD8(+) T Cells and Features of Hepatocellular Carcinoma. *Gastroenterology* **2018**;155(6):1936-50.e17 doi 10.1053/j.gastro.2018.08.030.
45. Murray PJ, Allen JE, Biswas SK, Fisher EA, Gilroy DW, Goerdts S, *et al.* Macrophage activation and polarization: nomenclature and experimental guidelines. *Immunity* **2014**;41(1):14-20 doi 10.1016/j.immuni.2014.06.008.
 46. Zhang B, Vogelzang A, Miyajima M, Sugiura Y, Wu Y, Chamoto K, *et al.* B cell-derived GABA elicits IL-10(+) macrophages to limit anti-tumour immunity. *Nature* **2021**;599(7885):471-6 doi 10.1038/s41586-021-04082-1.
 47. Fu Q, Xu L, Wang Y, Jiang Q, Liu Z, Zhang J, *et al.* Tumor-associated Macrophage-derived Interleukin-23 Interlinks Kidney Cancer Glutamine Addiction with Immune Evasion. *Eur Urol* **2019**;75(5):752-63 doi 10.1016/j.eururo.2018.09.030.
 48. Pardoll DM. The blockade of immune checkpoints in cancer immunotherapy. *Nat Rev Cancer* **2012**;12(4):252-64 doi 10.1038/nrc3239.
 49. Engblom C, Pfirschke C, Pittet MJ. The role of myeloid cells in cancer therapies. *Nat Rev Cancer* **2016**;16(7):447-62 doi 10.1038/nrc.2016.54.
 50. Cassetta L, Pollard JW. Targeting macrophages: therapeutic approaches in cancer. *Nat Rev Drug Discov* **2018**;17(12):887-904 doi 10.1038/nrd.2018.169.
 51. Lee M, Lee Y, Song J, Lee J, Chang SY. Tissue-specific Role of CX3CR1 Expressing Immune Cells and Their Relationships with Human Disease. *Immune Netw* **2018**;18(1):e5 doi 10.4110/in.2018.18.e5.
 52. Molgora M, Esaulova E, Vermi W, Hou J, Chen Y, Luo J, *et al.* TREM2 Modulation Remodels the Tumor Myeloid Landscape Enhancing Anti-PD-1 Immunotherapy. *Cell* **2020** doi 10.1016/j.cell.2020.07.013.
 53. Lee YS, Kim MH, Yi HS, Kim SY, Kim HH, Kim JH, *et al.* CX3CR1 differentiates F4/80(low) monocytes into pro-inflammatory F4/80(high) macrophages in the liver. *Sci Rep* **2018**;8(1):15076 doi 10.1038/s41598-018-33440-9.
 54. Pang L, Yeung OWH, Ng KTP, Liu H, Zhu J, Liu J, *et al.* Postoperative plasmacytoid dendritic cells secrete IFN- α to promote recruitment of myeloid-derived suppressor cells and drive hepatocellular carcinoma recurrence. *Cancer Res* **2022** doi 10.1158/0008-5472.Can-22-1199.
 55. Chiu DK, Xu IM, Lai RK, Tse AP, Wei LL, Koh HY, *et al.* Hypoxia induces myeloid-derived suppressor cell recruitment to hepatocellular carcinoma through chemokine (C-C motif) ligand 26. *Hepatology* **2016**;64(3):797-813 doi 10.1002/hep.28655.
 56. Yoshida H, Hunter CA. The immunobiology of interleukin-27. *Annu Rev Immunol* **2015**;33:417-43 doi 10.1146/annurev-immunol-032414-112134.
 57. Beizavi Z, Zohouri M, Asadipour M, Ghaderi A. IL-27, a pleiotropic cytokine for fine-tuning the immune response in cancer. *Int Rev Immunol* **2021**;40(5):319-29 doi 10.1080/08830185.2020.1840565.
 58. Cocco C, Giuliani N, Di Carlo E, Ognio E, Storti P, Abeltino M, *et al.* Interleukin-27 acts as multifunctional antitumor agent in multiple myeloma. *Clin Cancer Res* **2010**;16(16):4188-97 doi 10.1158/1078-0432.Ccr-10-0173.
 59. Morishima N, Owaki T, Asakawa M, Kamiya S, Mizuguchi J, Yoshimoto T. Augmentation of effector CD8+ T cell generation with enhanced granzyme B expression by IL-27. *J Immunol*

- 2005**;175(3):1686-93 doi 10.4049/jimmunol.175.3.1686.
60. Park YJ, Ryu H, Choi G, Kim BS, Hwang ES, Kim HS, *et al.* IL-27 confers a protumorigenic activity of regulatory T cells via CD39. *Proc Natl Acad Sci U S A* **2019**;116(8):3106-11 doi 10.1073/pnas.1810254116.
 61. Chihara N, Madi A, Kondo T, Zhang H, Acharya N, Singer M, *et al.* Induction and transcriptional regulation of the co-inhibitory gene module in T cells. *Nature* **2018**;558(7710):454-9 doi 10.1038/s41586-018-0206-z.
 62. Aghayev T, Mazitova AM, Fang JR, Peshkova IO, Rausch M, Hung MH, *et al.* IL27 Signaling Serves as an Immunologic Checkpoint for Innate Cytotoxic Cells to Promote Hepatocellular Carcinoma. *Cancer Discovery* **2022**;12(8):1960-83 doi 10.1158/2159-8290.Cd-20-1628.
 63. Yuan JM, Wang Y, Wang R, Luu HN, Adams-Haduch J, Koh WP, *et al.* Serum IL27 in Relation to Risk of Hepatocellular Carcinoma in Two Nested Case-Control Studies. *Cancer epidemiology, biomarkers & prevention : a publication of the American Association for Cancer Research, cosponsored by the American Society of Preventive Oncology* **2021**;30(2):388-95 doi 10.1158/1055-9965.Epi-20-1081.
 64. Wang Q, Li D, Cao G, Shi Q, Zhu J, Zhang M, *et al.* IL-27 signalling promotes adipocyte thermogenesis and energy expenditure. *Nature* **2021**;600(7888):314-8 doi 10.1038/s41586-021-04127-5.
 65. Ma RY, Black A, Qian BZ. Macrophage diversity in cancer revisited in the era of single-cell omics. *Trends Immunol* **2022** doi 10.1016/j.it.2022.04.008.
 66. Li H, Xiao Y, Li Q, Yao J, Yuan X, Zhang Y, *et al.* The allergy mediator histamine confers resistance to immunotherapy in cancer patients via activation of the macrophage histamine receptor H1. *Cancer Cell* **2022**;40(1):36-52 e9 doi 10.1016/j.ccell.2021.11.002.
 67. Bai Z, Ai J, Wei X. Histamine and histamine receptor H1 (HRH1) axis: new target for enhancing immunotherapy response. *Molecular Biomedicine* **2022**;3(1):11 doi 10.1186/s43556-022-00073-4.
 68. Nikolos F, Hayashi K, Hoi XP, Alonzo ME, Mo Q, Kasabyan A, *et al.* Cell death-induced immunogenicity enhances chemoimmunotherapeutic response by converting immune-excluded into T-cell inflamed bladder tumors. *Nat Commun* **2022**;13(1):1487 doi 10.1038/s41467-022-29026-9.
 69. Bell CR, Pelly VS, Moeini A, Chiang SC, Flanagan E, Bromley CP, *et al.* Chemotherapy-induced COX-2 upregulation by cancer cells defines their inflammatory properties and limits the efficacy of chemoimmunotherapy combinations. *Nat Commun* **2022**;13(1):2063 doi 10.1038/s41467-022-29606-9.

Figure Legends

Figure 1. Suboptimal anti-PD-1 therapy efficacy in Hepa1-6 orthotopic HCC

A-C, Representative *in vivo* luciferase imaging, tumor growth curve and tumor specimens from Hepa1-6-luci orthotopic HCC mice treated with anti-PD-1 mAb or IgG antibody (n = 6 mice per group). **D**, The proportion of CD8⁺ T cells among total CD45⁺ tumor-infiltrating immune cells in IgG or anti-PD-1 mAb treatment groups (n = 3 tumors per group at each time point). **E**, The content of IL-2 and IFN- γ in tumor tissues of IgG and anti-PD-1 mAb treatment groups (n = 3 tumors per group at each time point). **F**, Expression of functional molecules (IFN- γ , TNF- α , GZMB and PRF) on tumor-infiltrating CD8⁺ T cells in IgG and anti-PD-1 mAb treatment groups (n = 3 tumors per group at each time point). **G**, Expression of Immune checkpoint (LAG-3, TIGIT, TIM-3, PD-1) on tumor-infiltrating CD8⁺ T cells after 1st dose and 5th dose in IgG and anti-PD-1 treatment groups (n = 3 tumors per group at each time point). **H**, Representative flow cytometry plots showing PD-1 and TIM-3 expression on tumor-infiltrating CD8⁺ T cells in IgG and anti-PD-1 mAb treatment groups. **I**, Representative IF images of the T cell marker CD8, immune checkpoint markers PD-1 and TIM-3 in Hepa1-6-luci orthotopic HCC tissues (scaling: 20 \times and 40 \times). Two-way ANNOVA test was used to determine statistical significance at all timepoints. *, $P < 0.05$; **, $P < 0.01$; ***, $P < 0.001$; ****, $P < 0.0001$; ns, not significant. All data presented as mean \pm SD.

Figure 2. Accumulation of CX3CR1⁺ TAM during anti-PD-1 therapy

A-D, The proportion of distinct myeloid cell types (Neutrophil, Monocyte, Dendritic

cell and Macrophage) infiltrating the Hepa1-6-luci orthotopic tumors in IgG and anti-PD-1 mAb treatment groups (n = 3 tumors per group at each time point). **E-F**, Representative flow cytometry plots showing MHC II and CX3CR1 expression on TAMs in IgG and anti-PD-1 mAb treatment groups, along with their corresponding statistical charts (n = 3 tumors per group at each time point). **G**, Representative IF images of macrophage marker F4/80 and CX3CR1 expression in Hepa1-6 orthotopic HCC tissues from IgG and anti-PD-1 mAb treatment groups (scaling: 63×). **H**, Tumor infiltrating immune cells sorted from IgG or anti-PD-1 treatment group underwent scRNA-seq (cells from 5 tumors mixed into one sample per group). After data processing and clustering, TAMs (*Csf1r*⁺*CD68*⁺*Itgm*⁺) were selected and further subgrouped based on *Cx3cr1* expression. **I-J**, Key upregulated or downregulated KEGG pathways between CX3CR1⁺ and CX3CR1⁻ TAMs. **K**, Key GSEA enriched pathways in CX3CR1⁺ TAMs sorted from Hepa1-6-luci tumors treated with IgG or anti-PD-1 mAb. Two-way ANNOVA test was used to determine statistical significance at all timepoints. *, *P* < 0.05; **, *P* < 0.01; ***, *P* < 0.001; ****, *P* < 0.0001; ns, not significant. All data presented as mean ± SD.

Figure 3. Blocking CX3CR1 enhances anti-PD-1 therapy

A-B, The Hepa1-6-luci orthotopic tumor growth curve and representative tumor specimens from each treatment group (IgG, anti-PD-1, anti-CX3CR1 and anti-PD-1/anti-CX3CR1 combination, n = 6 mice per group). **C**, The survival curve of tumor-bearing mice in each treatment group (n = 13 mice per group). **D**, The proportion of different types of tumor-infiltrating immune cells in each treatment

group (n = 6 tumors per group). **E-F**, Expression of effector markers (CD69 and CD107a) and immune checkpoints (PD-1, TIM-3, LAG-3, TIGIT) on tumor-infiltrating CD8⁺ T cell in each treatment group (n = 6 tumors per group). **G**, Frequency of CX3CR1⁺ TAMs among total TAMs in each treatment group (n = 6 tumors per group). **H**, Representative IF images of macrophage marker F4/80 and CX3CR1 in tumor tissue from different treatment groups, along with their corresponding statistical charts (3 tumors per group, 3 fields per tumor, scaling: 63×). **I**, Frequency of Ki-67⁺ TAMs among total TAMs in each treatment group (n = 6 tumors per group). **J-K**, Representative IF images showing macrophage marker F4/80, proliferation marker Ki-67 (**J**) and apoptosis marker TUNEL (**K**) in each treatment group, along with their corresponding statistical charts (3 tumors per group, 3 fields per tumor, scaling: 63×). **L-M**, Control or CX3CR1^{OE} BMDMs were treated with 10 µg/ml CX3CR1-specific antibody for 48 hours. The proliferation marker Ki-67 and apoptosis marker Annexin V were subsequently detected by flow cytometry (n = 5 biological replicates per group). Data are presented as mean ± SD and analyzed by two-way ANOVA test (**A,E-F**), Log-rank test (**C**) and Tukey multiple comparisons test (**G-M**). Statistical significance indicated by *, $P < 0.05$; **, $P < 0.01$; ***, $P < 0.001$; ****, $P < 0.0001$; ns, not significant.

Figure 4. CX3CR1⁺ TAMs induce CD8⁺ T dysfunction via IL-27

A, Workflow for the *in vitro* co-culture of TAMs and CD8⁺ T cells. **B**, Comparison of cytokine secretion profiles between FACS sorted CX3CR1⁺ and CX3CR1⁻ TAMs (n = 5 biological replicates per group). **C-D**, Expression of immune checkpoint TIM-3 and

functional cytokines (TNF- α and IFN- γ) on CD8⁺ T cells under different co-culture conditions (n = 3 biological replicates per group, 2 independent experiments were performed). **E**, Workflow for the Winn assay using control or CX3CR1^{OE} BMDMs with Hepa1-6 cells. **F-G**, Tumor volume curve and representative tumor specimens from the Winn assay experiments (n = 7 mice per group). **H**, The proportion of different types of tumor-infiltrating immune cells in each Winn assay group (n = 6 tumors per group). **I**, Frequency of CX3CR1⁺ and Ki-67⁺ TAMs among total TAMs in each Winn assay group (n = 6 tumors per group). **J**, Expression of immune checkpoints (PD-1, TIM-3, LAG-3, TIGIT) on tumor-infiltrating CD8⁺ T cells in each Winn assay group (n = 6 tumors per group). **K-L**, Expression of effector markers (CD69 and CD107a) and functional cytokines (IFN- γ and TNF- α) on tumor-infiltrating CD8⁺ T cells in different Winn assay groups (n = 6 tumors per group). Workflow diagrams (**A**, **E**) were drawn by Figdraw. Data are presented as mean \pm SD and analyzed using unpaired two-tailed *t* test (**B**), Tukey multiple comparisons test (**C-D**) and two-way ANOVA test (**F**, **I-L**). Statistical significance indicated by *, *P* < 0.05; **, *P* < 0.01; ***, *P* < 0.001; ****, *P* < 0.0001; ns, not significant.

Figure 5. PGE2 derived from Immune-attacked tumor cells promotes CX3CR1 upregulation on macrophages

A, Expression of CX3CR1 on BMDMs after exposure to various stimuli for 48 hours (n = 4 biological samples per group, 2 independent experiments were performed). **B**, Workflow for immune attack experiment and subsequent testing. **C**, PCA plot of

metabolomics results in the supernatant of immune attack experiments (n = 4 biological replicates per group). **D**, Volcano plot of differential metabolites in the supernatant from immune-attacked tumor cells compared to that from normal tumor cells (n = 4 biological replicates per group). **E**, KEGG pathway analysis of differential metabolites suggested that the arachidonic acid (AA) metabolism pathway is enriched in the supernatant derived from immune attacked tumor cells (n = 4 biological replicates per group). **F**, GSEA pathway analysis of bulk RNA-seq data from tumor cells indicates enrichment of arachidonic acid metabolism pathway in immune-attacked tumor cells (n = 5 biological replicates per group). **G**, Western blot and qPCR suggested upregulation of arachidonic acid metabolism-related enzymes (COX-2 and mPGES-1) in immune-attacked Hepa1-6 cells. For western blot, 3 independent experiments were performed. For qPCR, 4 biological replicates were tested. **H**, Expression of CX3CR1 on BMDMs after exposure to different stimuli for 48 hours (n = 3 biological replicates per group, 2 independent experiments were performed). **I**, Expression of CX3CR1 on BMDMs stimulated with 10 μ M PGE2 in the presence or absence of 10 μ M prostaglandin receptor (EP2 or EP4) inhibitors (n = 4 biological replicates per group, 2 independent experiments were performed). Workflow diagrams (**B**) were drawn by Figdraw. Data are presented as mean \pm SD and analyzed using Tukey multiple comparisons test (**A**, **H-I**) and unpaired two-tailed *t* test (**D-E**, **G**). Statistical significance indicated by *, $P < 0.05$; **, $P < 0.01$; ***, $P < 0.001$; ****, $P < 0.0001$; ns, not significant.

Figure 6. Blocking PGE2 release synergizes with the efficacy of anti-PD-1

therapy

A-C, Representative *in vivo* luciferase imaging, tumor growth curve and tumor specimens in different treated orthotopic Hepa1-6-luci tumors (IgG, anti-PD-1, Celecoxib and Celecoxib/anti-PD-1 combination, n = 6 mice per group). **D-E**, PGE2 content in peripheral blood and tumor tissues in different treatment groups (n = 4 biological replicates per group). **F**, The proportion of CX3CR1⁺ TAMs among total TAMs in different treatment groups, along with their corresponding statistical chart (n = 5 tumors per group). **G-H**, Expression of immune checkpoints (PD-1, TIM-3, LAG-3 and TIGIT) and functional cytokines (IFN- γ , TNF- α , PRF and GZMB) on tumor-infiltrating CD8⁺ T cell in different treatment groups (n = 4 tumors per group). Data are shown as mean \pm SD and analyzed using two-way ANOVA test (**B**, **G-H**) and Tukey multiple comparisons test (**D-F**). Statistical significance indicated by *, $P < 0.05$; **, $P < 0.01$; ***, $P < 0.001$; ****, $P < 0.0001$; ns, not significant.

Figure 7. High CX3CR1⁺ TAM infiltration and serum PGE2 levels correlate with suboptimal efficacy of immunotherapy

A, Representative IHC images depicting high and low infiltration of CX3CR1⁺ TAM in HCC patients undergoing neoadjuvant anti-PD-1 therapy (scaling: 20 \times and 40 \times). **B**, Survival curve for RFS of patients with high or low CX3CR1⁺ TAM infiltration (n = 7 patients per group, log-rank $P = 0.0118$). **C**, Comparison of preoperative serum PGE2 levels in patients with stable disease (SD) or progressive disease (PD) within 6 months after surgery (SD, n = 8 patients; PD, n = 6 patients). **D**, Survival curve

representing RFS of patients with high and low preoperative PGE2 levels (n = 7 patients per group, log-rank $P = 0.0174$). **E**, Dynamic changes in peripheral blood PGE2 levels in HCC patients with partial response (PR)/SD (n = 10 patients) and PD (n = 6 patients) within 6 months of receiving anti-PD-1 based immunotherapy. **F**, Heatmap visualizing the association between CX3CR1⁺ TAM-related signatures and various components of TME in the HCC immunotherapy cohort (ERP117672, GSE202069). **G**, Sankey plot depicting association of CX3CR1⁺ TAM-related signatures with immunotherapy responsiveness among HCC patients (ERP117672, GSE202069). **H-J**, *Cx3cr1-Ptgs2* dual-gene signature is significantly associated with overall survival (OS) and progress free survival (PFS) in HCC patients receiving immunotherapy (GSE140901). Data are shown as mean \pm SD and analyzed by log-rank test (**B**, **D**, **H-I**), unpaired two-tailed *t* test (**C**) and two-way ANOVA test (**E**).

Figure 1.

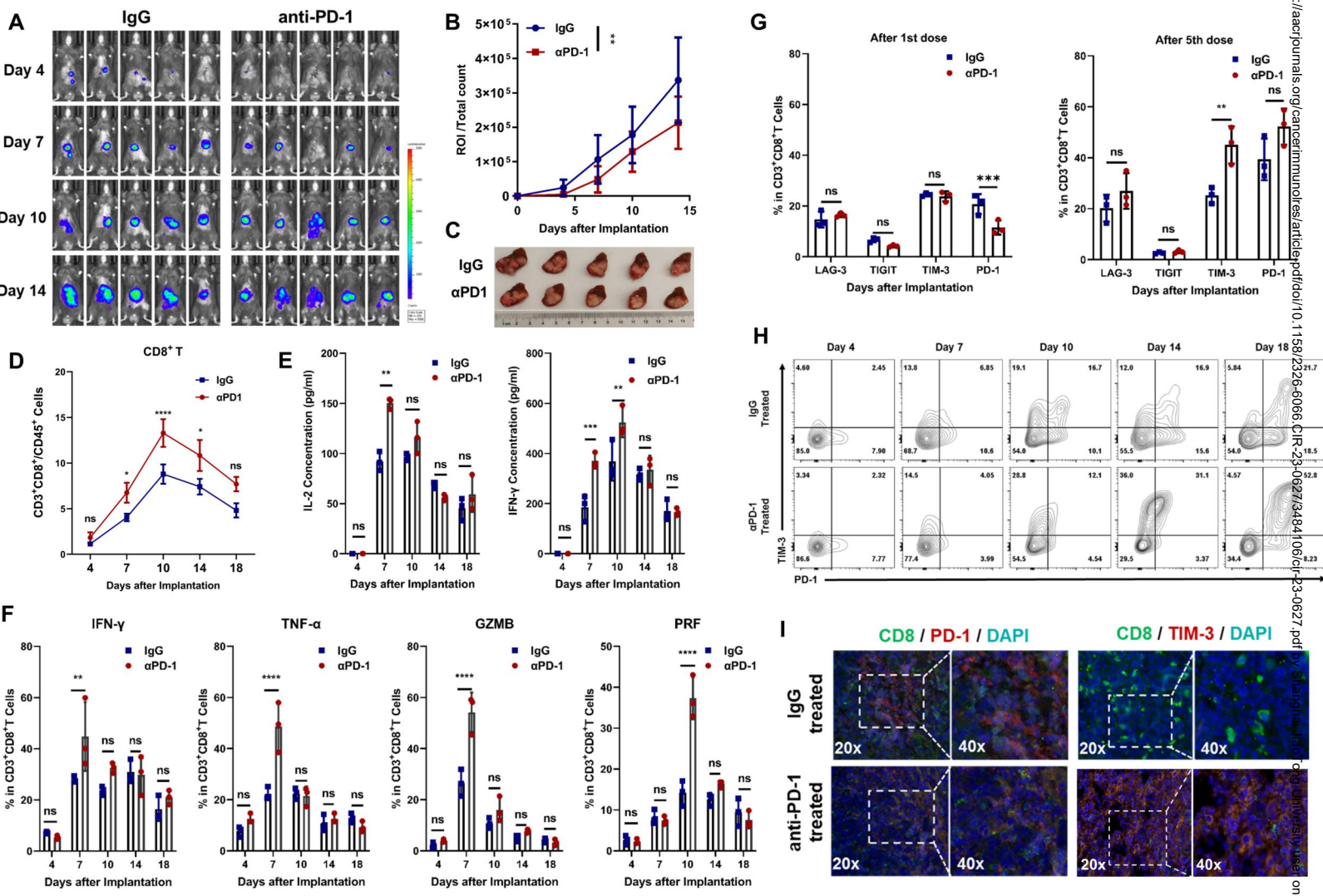


Figure 2.

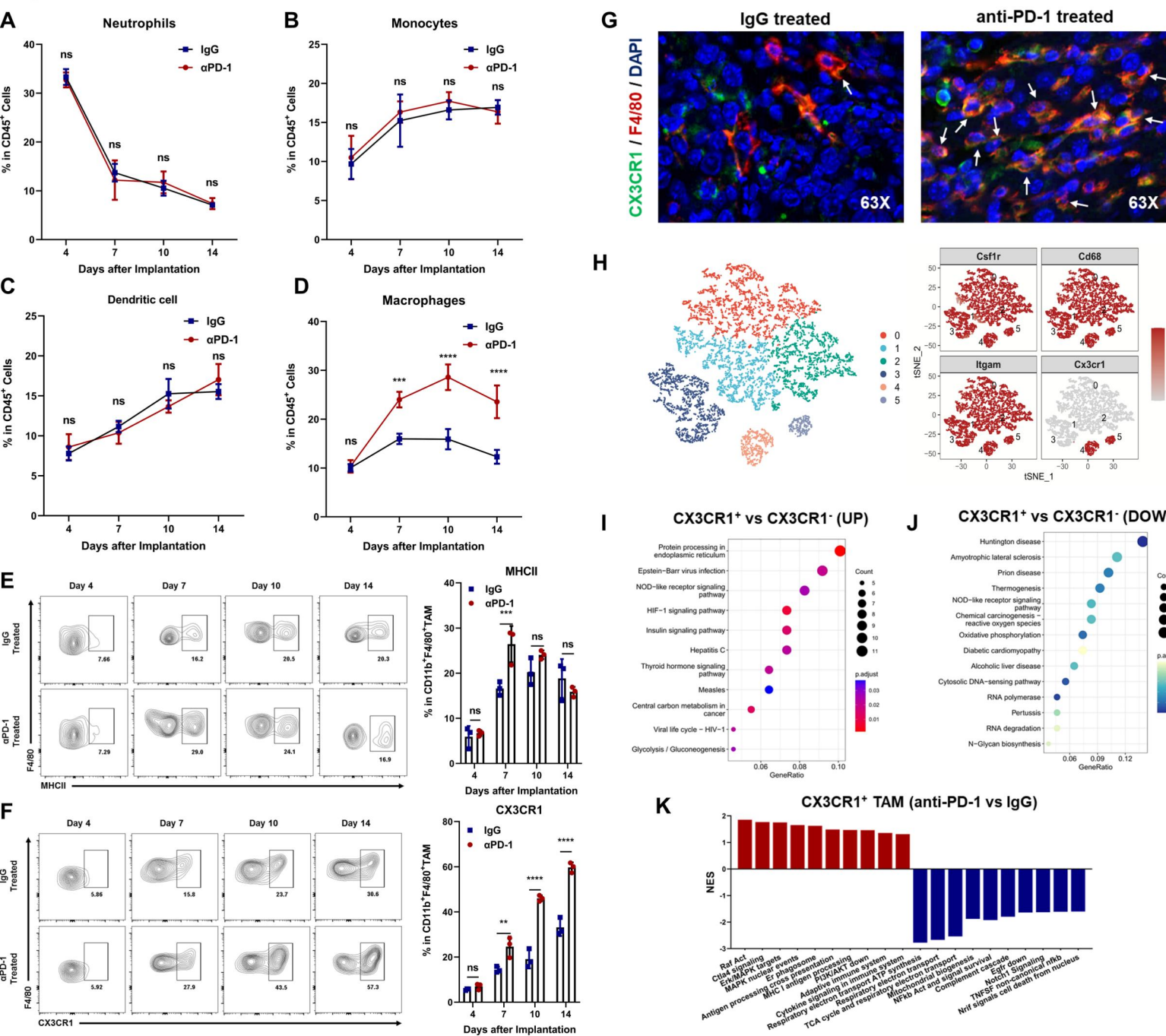


Figure 3.

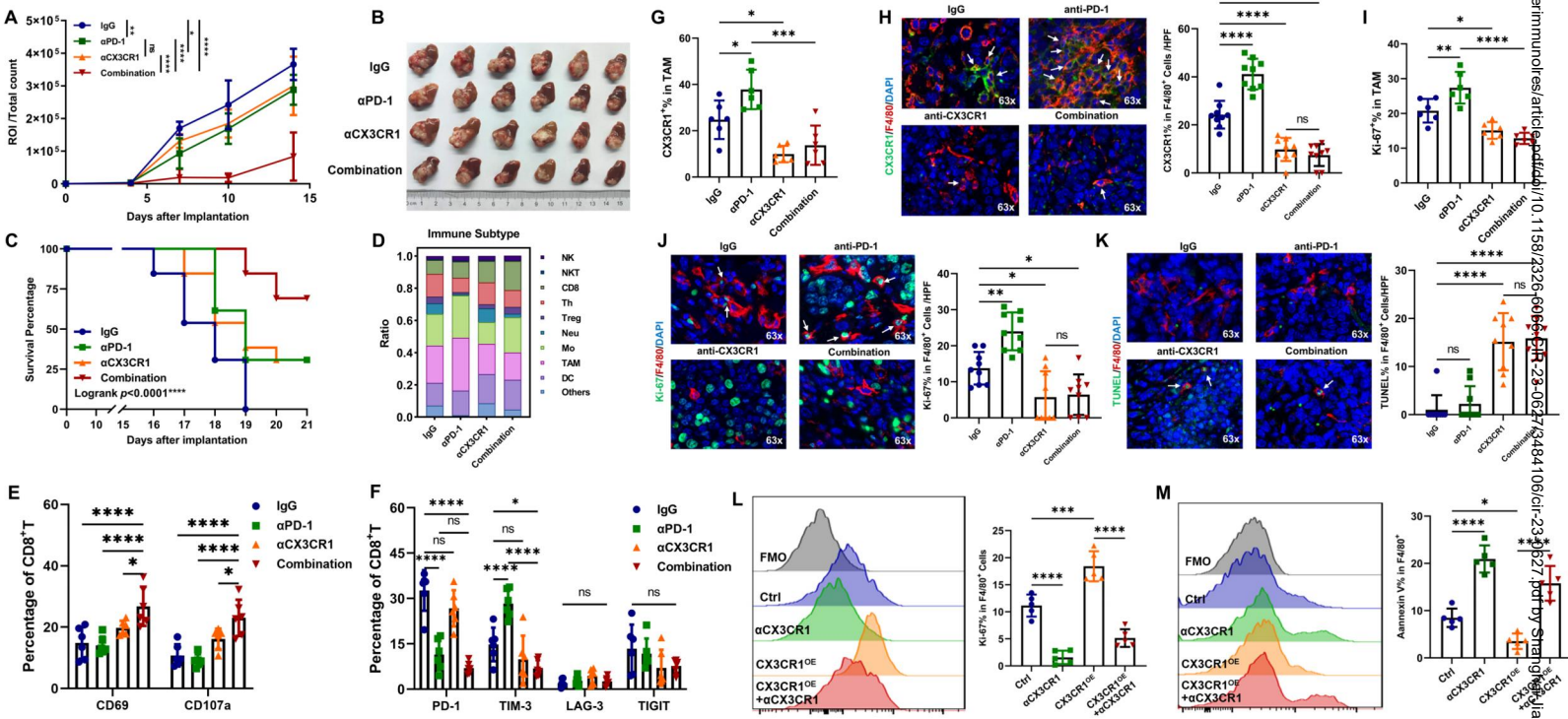


Figure 4.

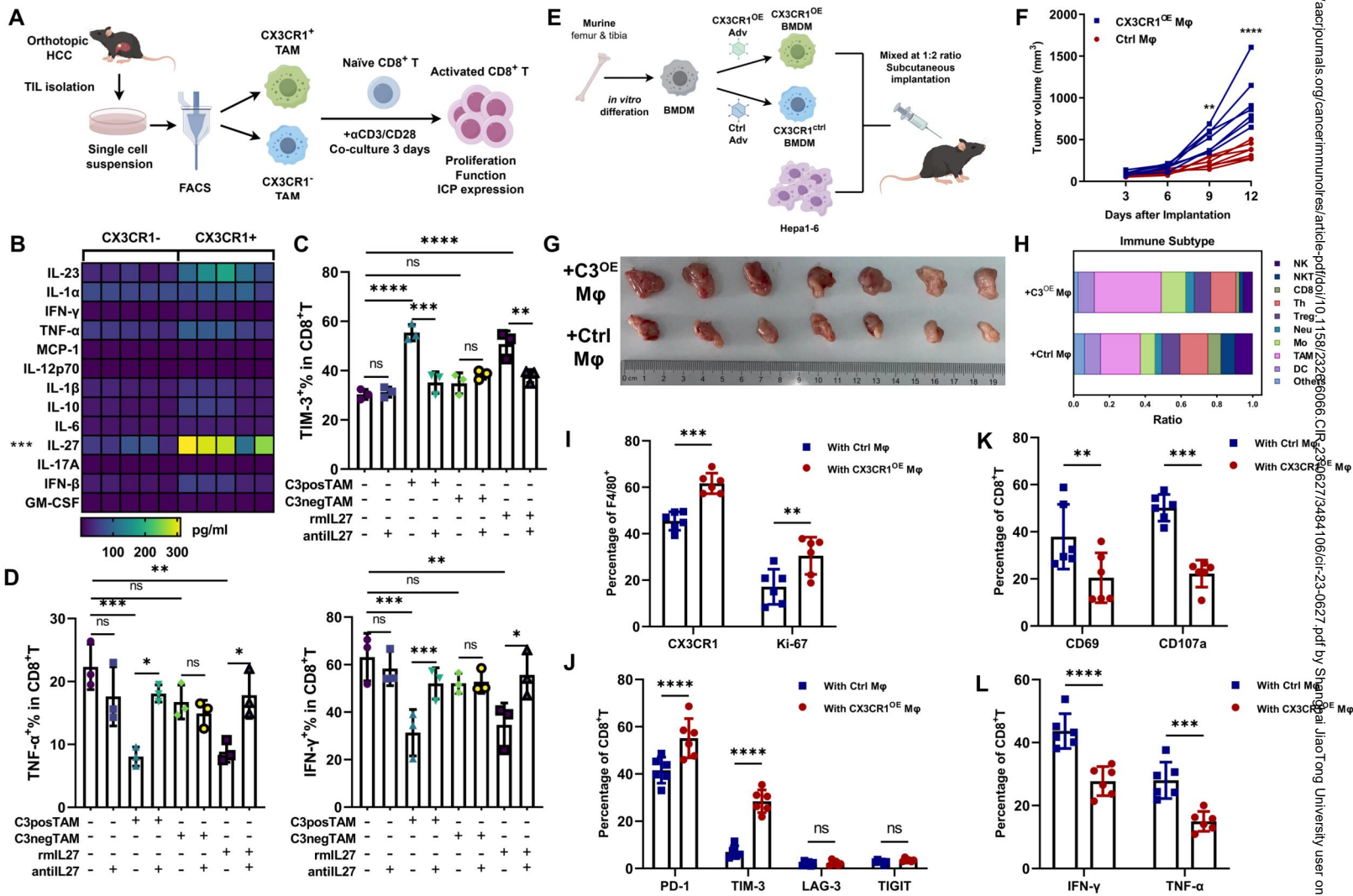


Figure 5.

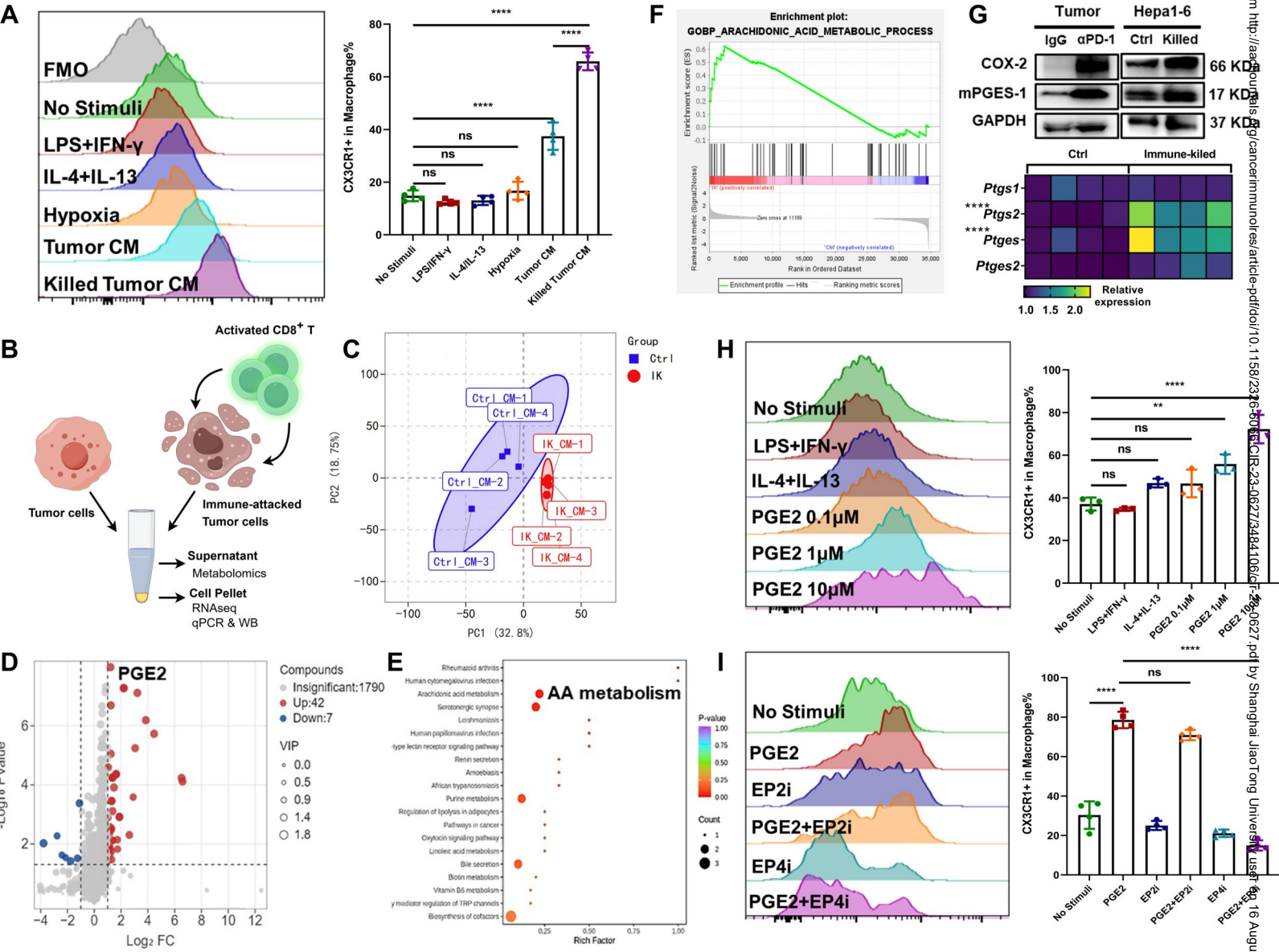


Figure 6.

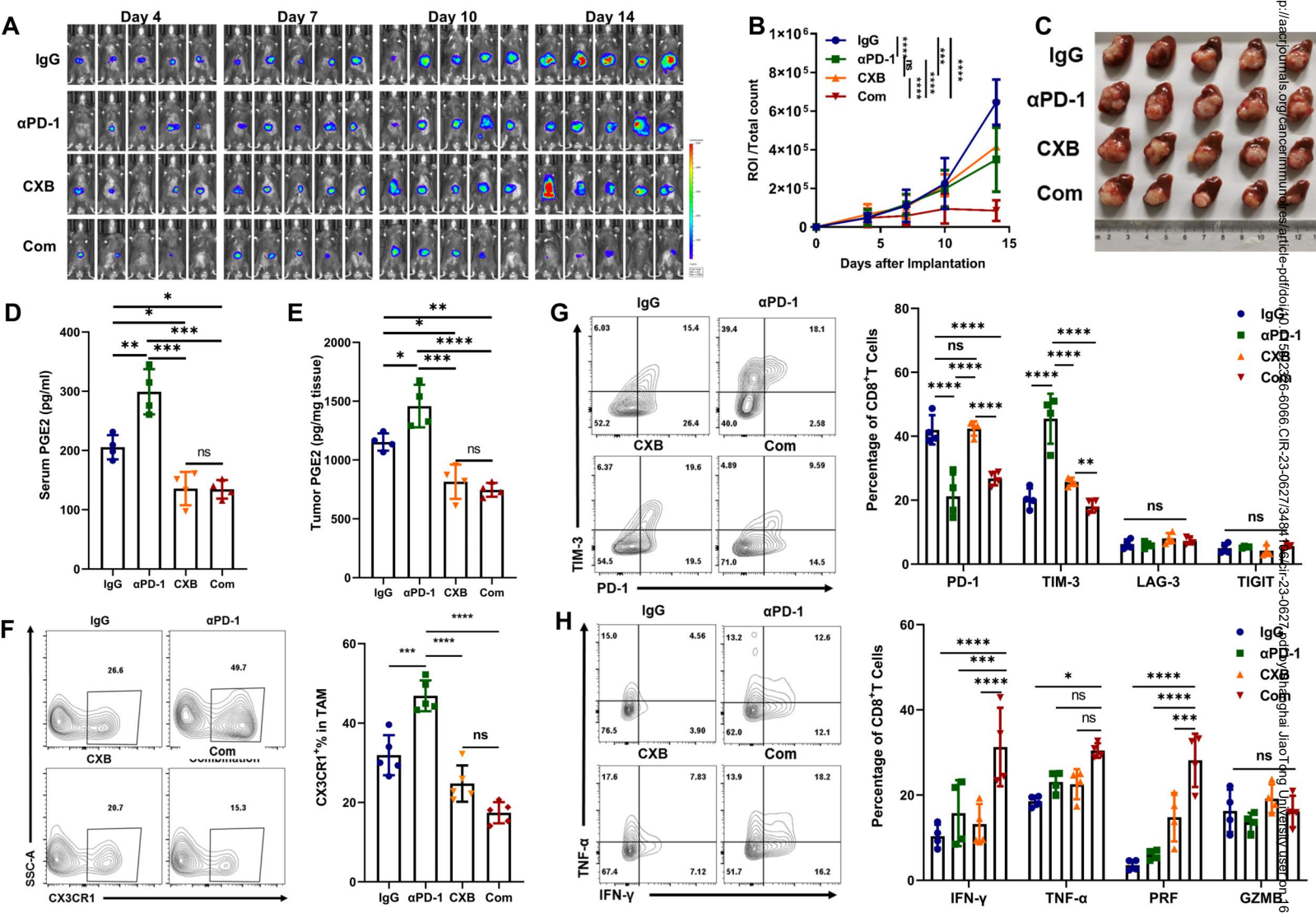


Figure 7.

